Intelligent Tracking Control System for Fast Image Scanning of Atomic Force Microscopes

Sajal K. Das, Hemanshu R. Pota and Ian R. Petersen

Abstract Atomic force microscope (AFM) is a type of scanning probe microscopy technique which is used to measure the characteristics of various specimens at an atomic level through surface imaging. In the imaging process of the AFM the sample is placed on a positioning unit termed as nanopositioner. The performance of the AFM for fast image scanning is limited to the one percent of the first resonance frequency of its positioning unit. Many imaging applications require a faster response and high quality imaging than what can be achieved using the currently available commercial AFMs. The need for high speed imaging is the reduction of the computational time to capture an image. The time require to capture an image of a reference grating sample for an 8 μm × 8 μm area and 256 number of scan lines at the scanning rate of 1 Hz and 125 Hz are 170s and 2 s. This shows the importance of the increase of scan frequency in terms of operation time. The tracking performance of the nanopositioner of the AFM for high speed imaging is limited due to the vibration of the nanopositioner, cross coupling effect between the axes of the nanopositioner and nonlinear effects in the form of hysteresis and creep. In this chapter we have proposed an intelligent multi-variable tracking controller to compensate the effect of vibration, cross coupling and nonlinearities in the form of hysteresis and creep in AFM for fast image scanning. Experimental results in time and frequency domain are presented to show the effectiveness of the proposed controller.

Keywords Piezoelectric tube scanner · Atomic force microscope · Negative-imaginary systems · Passive systems · Resonant controller · Vibration control

S.K. Das (✉) · H.R. Pota · I.R. Petersen
School of Engineering and Information Technology (SEIT), The University of New South Wales, Canberra 2600, ACT, Australia
e-mail: das.k.sajal@gmail.com

H.R. Pota
e-mail: h.pota@adfa.edu.au

I.R. Petersen
e-mail: i.r.petersen@gmail.com

© Springer International Publishing Switzerland 2015

A.T. Azar and S. Vaidyanathan (eds.), *Chaos Modeling and Control Systems Design*,
Studies in Computational Intelligence 581, DOI 10.1007/978-3-319-13132-0_14

1 Introduction

Nanotechnology is the branch of science which deals with the manipulation of matters on an extremely atomic level. Nanotechnology as defined by size is naturally very broad, including fields of science as diverse as surface science, organic chemistry, molecular biology, semiconductor physics, and microfabrication. The viewing of surface texture at the atomic level with extremely high resolution was a great challenge until the introduction of the scanning tunneling microscope (STM) [12–15]. The STM was developed by Gerd Binning and his colleagues in 1981 at the IBM Zurich Research Laboratory in Switzerland [12, 13]. The STM was the first SPM technique capable of directly obtaining three-dimensional (3-D) images of solid surfaces. The discovery of the STM has brought Nobel Prize to Binning and Rohrer in Physics in 1986. The STM is only used to measure the topography of surfaces which are electrically conductive to some degree. This limits the use of the STM for the surfaces which are non-conductive in nature. The invention of the AFM has opened a new era to the field of nanotechnology to study non-conductive sample surfaces. The AFM is used to measure the topography of any engineering surface, whether it is electrically conductive or insulating. The invention of the AFM has also led to the invention of the family of scanning probe microscopy techniques (SPMs). These include scanning electrostatic force microscopy (SEFM) [61], scanning force acoustic microscopy (SFAM) (or atomic force acoustic microscopy (AFAM)) [3, 53], magnetic force microscopy (MFM) [58, 31], scanning near field optical microscopy (SNOM) [8, 7], scanning thermal microscopy (SThM) [40, 63], scanning electromechanical microscopy (SEcM) [33], scanning Kelvin probe microscopy (SKPM) [24, 43], scanning chemical potential microscopy (SCPM) [64], scanning ion conductance microscopy (SICM) [30, 49] and scanning capacitance microscopy (SCM) [37, 41]. The reason for calling them as SPM is because of using probe in these devices for investigation and manipulation of matters. The commercial use of the SPM was started in 1987 with the STM and 1989 with the AFM by Digital Instruments Inc. The basic stage for the development of the SPM systems is as follows:

1. 1981—*Scanning tunneling microscope*. G. Binning ang H. Rohrer. Atomic resolution images of conducting surfaces.
2. 1982—*Scanning near-field optical microscope*. D.W. Pohl. Resolution of 50 nm in optical images
3. 1984—*Scanning capacitive microscope*. J.R. Matey, J. Blanc. 500 nm (lateral resolution) images of capacitance variation.
4. 1985—*Scanning thermal microscope*. C.C. Williams, H.K. Wickramasinghe. Resolution of 50 nm in thermal images.
5. 1986—*Atomic force microscope*. G. Binning, C.F. Quate, Ch. Gerber. Atomic resolution on non-conducting (and conducting) samples.
6. 1987—*Magnetic force microscope*. Y. Martin, H.K. Wickramasinghe. Resolution of 100 nm in magnetic images.

7. 1988—*Inverse photoemission microscope*. J.H. Coombs, J.K. Gimzewski, B. Reihl, J.K. Sass, R.R. Schlittler. Detection of luminescence spectra on nanometer scales.
8. 1989—*Near-field acoustic microscope*. K. Takata, T. Hasegawa, S. Hosaka, S. Hosoki, T. Komoda. Low frequency acoustic measurements with the resolution of 10 nm.
9. 1990—*Scanning chemical potential microscope*. C.C. Williams, H.K. Wickramasinghe. Atomic scale images of chemical potential variation.
10. 1991—*Kelvin probe force microscope*. N. Nonnenmacher, M. P. O'Boyle, H K. Wickramasinghe. Measurements of surface potential with 10 nm resolution.
11. 1994—*Apertureless near-field optical microscope*. F. Zenhausern, M.P. O'Boyle, H.K. Wickranmasinghe. Optical microscopy with 1 nm resolution.

2 Operating Principle of the AFM

Atomic force microscope (AFM) is a very high-resolution type of scanning probe microscope with demonstrated resolution on the order of fractions of a nanometer. Despite of the great success of the STM it was obvious that STM has a fundamental disadvantage. The STM can investigate only the conductive or semi-conductive samples. This disadvantage was overcome due to the invention of the AFM. Like the STM, the AFM relies on a scanning technique to produce very high resolution 3-D images of sample surfaces. The AFM is based upon the principle of sensing the forces between a sharp tip and the surface to be investigated. The forces can be attractive or repulsive depending on the operating modes. When tip to sample distance is large the interactive force is attractive and when the tip to sample distance is small the interactive force is repulsive. The forces are measured by measuring the motion of a very small cantilever beam. During the operation of the AFM the sample is scanned instead of the tip (unlike the STM) because the AFM measures the relative displacement between the cantilever surface and the reference surface.

A schematic of the AFM is presented in Fig. 1. The basic components include a micro-cantilever with a sharp tip mounted on a micromachined cantilever, a positioning unit, a laser source, and a laser photodetector. In the imaging process of the AFM, a sample is placed on a positioning unit. There are different types of positioning units used in the AFM such as piezoelectric tube scanner, serial-kinematic scanner, flexure based scanners. The use of the positioning unit depends on the application of the AFM. A detail discussion on the various types of the positioning unit used in the AFM is discussed later. The displacement of the positioning unit during the imaging is measured by sensor. In most of the cases capacitive sensors are used to measure the displacement of the scanner.

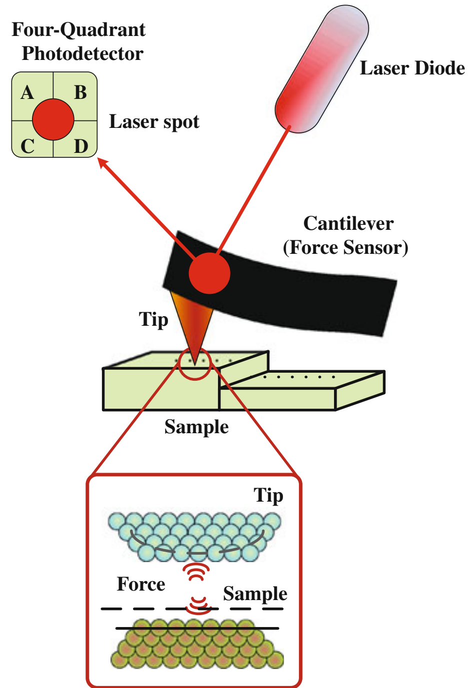

Fig. 1 Block diagram of the AFM working principle

When the sample is placed on the positioning unit, a cantilever beam with a sharp tip is brought in the close proximity of the sample. Various types of cantilevers are used in the AFM. The cantilever used in the AFM should meet the following criteria: (1) low normal spring constant (stiffness); (2) high resonant frequency; (3) high cantilever quality factor Q; (4) high lateral spring constant (stiffness); (5) short cantilever length; (6) incorporation of components (such as mirror) for deflection sensing; and (7) a sharp protruding tip. The cantilever used in the AFM system also has different shape. But in most of the cases a tip is attached with the cantilever.

In order to achieve the large imaging bandwidth the cantilever should have a high resonant frequency. The Young's modulus and the density are the material parameters that determine the resonant frequency, aside from the geometry. This makes the cantilever the least sensitive part of the system. In order to register a measurable deflection with small forces it is also required that the cantilever should have low spring constant. The combined requirement of having high resonance frequency and low spring constant is meet by reducing the mass of the cantilever. The tip used with the cantilever should have radius much smaller than the radii of the corrugations in the sample in order for these to be measured accurately. The cantilever is typically silicon or silicon nitride with a tip radius of curvature on the order of nanometers. Silicon nitride cantilevers are less expensive. They are very rugged and well suited to

imaging in almost all environments. They are especially compatible with organic and biological materials.

The most common methods to detect cantilever deflections are the optical lever method, the interferometric method, and the electronic tunneling method. The optical lever method is the most used one, since it is the most simple to implement. It consists in focusing a laser beam on the back side of the cantilever and in detecting the reflected beam by means of a position sensor, that is usually a quartered photodiode. Both cantilever deflection and torsion signals may be collected.

When the sample is placed on the positioning unit of the AFM, the cantilever is placed in the close contact of the sample. In this process an electric field is applied across the positioning unit of the AFM. This induces a displacement of the positioning unit. The displacement of the positioning unit is measured using sensor such as capacitive sensor. A laser beam is transmitted to and reflected from the cantilever for measuring the cantilever orientation. The reflected laser beam is detected with a position-sensitive detector consisting of two closely spaced photodiodes whose output signal is collected by a differential amplifier. In most of the cases the photo detector has four quadrants. A photodiode is a type of photodetector capable of converting light into either current or voltage, depending upon the mode of operation. The output of the photodetector is provided to a computer for processing of the data for providing a topographical image of the surface with atomic resolution. Currently used position-sensitive detectors are four-sectional that allows measuring not only longitudinal but torsion bending too.

3 Operating Modes of the AFM

The operating mode of the AFM can be classified into different types depending on the different measurement parameters used in sensing the interactive forces. Three basic fundamental operating modes of the AFM are: (1) contact mode; (2) non-contact mode; and (3) tapping mode.

3.1 Contact Mode

In contact mode the tip of the cantilever is placed in contact with the sample. This mode is the most common mode used in the AFM. The force acting on this mode is repulsive force in the order of 10^{-9}. The force is set by pusing the cantilever against the sample surface. In this mode the deflection of the cantilever is first sensed and than compared to some desired value of the deflection. Repulsion force F acting upon the tip is related to the cantilever deflection value x under Hooke's law: $F = -kx$, where k is cantilever spring constant. The spring constant value for

different cantilevers usually vary from 0.01 to several N/m. The deflection of the cantilever is converted into electrical signal DFL. The DFL signal is used to characterized the interaction force between the tip and the surface.

During contact mode when the atoms are gradually brought together, they first weakly attract each other. This attraction increases until the atoms are so close together that their electron clouds begin to repel each other electrostatically. This electrostatic repulsion progressively weakens the attractive force as the interatomic separation continues to decrease. The force goes to zero when the distance between the atoms reaches a couple of Angstroms, about the length of a chemical bond. When the total Van der Waals force becomes positive (repulsive), the atoms are in contact.

The slope of the Van der Waals curve is very steep in the repulsive or contact regime. As a result, the repulsive Van der Waals force balances almost any force that attempts to push the atoms closer together. In AFM this means that when the cantilever pushes the tip against the sample, the cantilever bends rather than forcing the tip atoms closer to the sample atoms. Two other forces are generally present during contact AFM operation: a capillary force exerted by the thin water layer often present in an ambient environment, and the force exerted by the cantilever itself. The capillary force arises when water surrounds the tip, applying a strong attractive force (about 10^{-8} N) that holds the tip in contact with the surface. The magnitude of the capillary force depends upon the tip-to-sample separation. The force exerted by the cantilever is like the force of a compressed spring. The magnitude and sign (repulsive or attractive) of the cantilever force depends upon the deflection of the cantilever and upon its spring constant.

As long as the tip is in contact with the sample, the capillary force should be constant because the distance between the tip and the sample is virtually incompressible. It is assumed that the water layer is reasonably homogeneous. The variable force in contact AFM is the force exerted by the cantilever. The total force that the tip exerts on the sample is the sum of the capillary plus cantilever forces, and must be balanced by the repulsive Van der Waals force for contact AFM. The magnitude of the total force exerted on the sample varies from 10^{-8} to the more typical operating range of $10^{-7}$to 10^{-6}. Most AFMs detect the position of the cantilever with optical techniques. In the most common scheme, a laser beam bounces off the back of the cantilever onto a position-sensitive photodetector (PSPD). As the cantilever bends, the position of the laser beam on the detector shifts. The PSPD itself can measure displacements of light as small as 10 Å. The ratio of the path length between the cantilever and the detector to the length of the cantilever itself produces a mechanical amplification. As a result, the system can detect sub-Angstrom vertical movement of the cantilever tip.

If the deflection of the cantilever is not matched with the predefined value of the deflection a voltage across the positioning unit of the AFM is applied to raise or lower the sample relative to the cantilever to restore the desired value of deflection. The voltage that the feedback amplifier applies to the positioning unit is a measure of the height of features on the sample surface. The predefined value of the cantilever deflection depends on operating modes. Two types of modes are used in

contact mode atomic force microscopy, (a) constant force mode; and (b) constant height mode. In constant force mode the force between the tip and sample remains fixed. This means that the deflection of the cantilever remains fixed. By maintaining a constant cantilever deflection (using the feedback loops) the force between the probe and the sample remains constant and an image of the surface is obtained. In this mode vertical deflection, i.e. the control voltage applied to Z electrode is measured. The vertical deflection is used to plot the surface topography. The advantage of the constant force mode is that this method allows to measure the surface topography with high resolution. Constant force mode is good for rough samples, used in friction analysis.

Constant force mode also has some disadvantages. The scanning speed of the AFM in constant force mode is restricted by the response time of feedback system. The soft samples such as polymers and biological samples can be destroyed due to interaction between the sharp probe and sample. The local flexure of the soft sample surfaces may be varied. The existence of the substantial capillary forces between the probe and the sample can decrease the resolution as well.

During scanning at constant height mode the distance between the tip of the cantilever and sample remains fixed. The cantilever base moves at a constant height from the sample surface. In constant-height mode, the spatial variation of the cantilever deflection can be used directly to generate the topographic data set because the height of the scanner is fixed as it scans. The main advantage of the constant height mode is high scanning speeds. The scanning speed at constant height mode is restricted only by resonant frequency of the cantilever. Constant height mode also has some disadvantages. In constant height mode the samples are required to be sufficiently smooth. The soft sample can be destroyed because the tip is in direct contact with the surface of the sample.

The operation of the contact mode atomic force microscopy is described in Fig. 2 by force versus distance curve. The line in Fig. 2 indicates the position of the cantilever. The flat line indicates that the cantilever is away from the sample. When

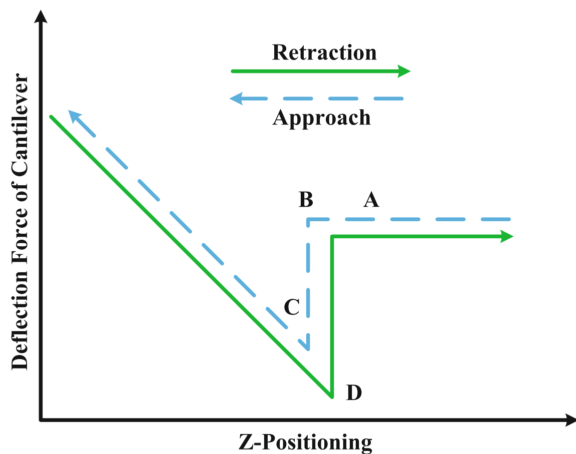

Fig. 2 Force versus distance curve in contact mode of the AFM imaging

cantilever approaches to the sample an attractive force is generated as shown in the point A. The point B indicates that the cantilever touches the sample surface. At point C the tip of the cantilever approaches further to the sample. At this point a repulsive force is generated to deflect the cantilever away from the sample. Again during the retraction period of the sample an attractive force is generated as shown by point D.

3.2 Non-contact Mode

In non-contact mode the probe does not contact the sample surface, but oscillates above the adsorbed fluid layer on the surface during scanning. This mode belongs to a family of modes which refers to the use of an oscillating cantilever. The non-contact mode is used in situations where tip contact might alter the sample in subtle ways. In this mode the tip hovers 50–150 Å above the sample surface. Normally the cantilever used in the non-contact mode has higher stiffness and high spring constant in the order of 10–100 Nm^{-1}. This is to avoid sticking to the sample surface. The forces between the tip and sample are quite low, on the order of pN (10^{-12} N). In this mode the cantilever is usually vibrated at its resonant frequency. The amplitude of the oscillation is kept less than 10 nm. Attractive Van der Waals force is acted between the tip and sample. This attractive force is substantially weaker than the forces used by contact mode. That is why the tip is given a small oscillation so that the AC detection methods can be used to detect the small forces between the tip and the sample. This is done by measuring the change in amplitude, phase, or frequency of the oscillating cantilever in response to force gradients from the sample. The detection scheme is based on measuring changes to the resonant frequency or amplitude of the cantilever due to its interaction with the sample.

The imaging resolution using non-contact mode depends of the distance between tip-sample. The tip-sample distance could be reduced further to achieve AFM images with high resolution. This can also be achieved in ultra-high vacuum (UHV) environment instead of in ambient condition. One of the limitation of operating AFM in ambient condition is that the tip-sample must be set at a larger distance to avoid tip from being trapped in the ambient water layer on the sample surface. Non-contact mode of the AFM is classified into two catagories, namely amplitude modulation (AM) and and frequency modulation (FM). In amplitude modulation mode an external signal with constant amplitude and phase is applied to the piezo actuator of the cantilever to excite and vibrate the cantilever. In this mode the amplitude of the cantilever is affected by the repulsive force acting on the tip during the operation. In frequency modulation mode the cantilever is always excited to vibrate at its resonance frequency. The advantage of the non-contact mode is that in this mode a very low force is exerted on the sample about 10^{-12} N. This extends the lifetime of the probe. The non-contact mode usually results in lower resolution; contaminant layer on surface can interfere with oscillation; usually need ultra high vacuum (UHV) to have best imaging.

3.3 Tapping Mode

The tapping mode is also called as semi-contact mode. This is an important mode in the AFM imaging. This is because this method allows for a high resolution imaging of sample surfaces that are easily damaged, loosely hold to their substrate, or difficult to image by other AFM techniques. In this mode the cantilever is oscillated at its resonant frequency. Tapping mode overcomes problems associated with friction, adhesion and other difficulties. This is done by alternatively placing the tip in contact with the surface to provide high resolution. Then the tip is lifted off surface to avoid dragging the tip across the sample. The oscillation of the cantilever in tapping mode is done using a piezoelectric crystal at the base of the cantilever. When the piezoelectric crystal comes into motion the cantilever oscillates. The amplitude of the oscillation of the cantilever is nearly in the order of 20 nm.

Selection of the optimal oscillation frequency is software-assisted and the force on the sample is automatically set and maintained at the lowest possible level. When the tip passes over a bump in the surface, the cantilever has less room to oscillate and the amplitude of oscillation decreases. Conversely, when the tip passes over a depression, the cantilever has more room to oscillate and the amplitude increases. The oscillation amplitude of the tip is measured by the detector and input to the controller electronics. The digital feedback loop then adjusts the tip-sample separation to maintain a constant amplitude and force on the sample.

During scanning, the vertically oscillating tip alternately contacts the surface and lifts off, generally at a frequency of 50,000–500,000 cycles per second. As the oscillating cantilever begins to intermittently contact the surface, the cantilever oscillation is necessarily reduced due to energy loss caused by the tip contacting the surface. The reduction in oscillation amplitude is used to identify and measure surface features.

Tapping mode inherently prevents the tip from sticking to the surface and causing damage during scanning. Unlike contact and non-contact modes, when the tip contacts the surface, it has sufficient oscillation amplitude to overcome the tip-sample adhesion forces. Also, the surface material is not pulled sideways by shear forces since the applied force is always vertical. Another advantage of the tapping mode technique is its large, linear operating range. This makes the vertical feedback system highly stable, allowing routine reproducible sample measurements.

Tapping mode operation in fluid has the same advantages as in the air or vacuum. However imaging in a fluid medium tends to damp the cantilever's normal resonant frequency. In this case, the entire fluid cell can be oscillated to drive the cantilever into oscillation. This is different from the tapping or non-contact operation in air or vacuum where the cantilever itself is oscillating. When an appropriate frequency is selected (usually in the range of 5,000–40,000 cycles per second), the amplitude of the cantilever will decrease when the tip begins to tap the sample, similar to Tapping Mode operation in air. Alternatively, the very soft cantilevers can be used to get the good results in fluid. The spring constant is typically 0.1 N/m compared to the tapping mode in air where the cantilever may be in the range of 1–100 N/m.

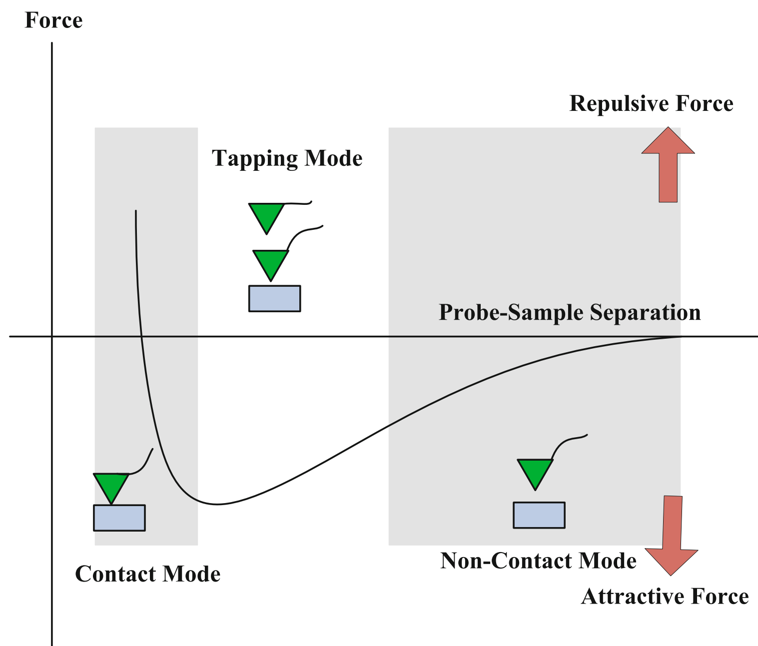

Fig. 3 Plot of force as a function of probe-sample separation

The description of three modes of the AFM in terms of force versus probe-sample distance is shown in Fig. 3. The dominant force acted at the short probe-sample distance in the AFM is the Van der Waals force. Long-range interactions such as capillary, electrostatic, magnetic are significant further away from the surface. During contact with the sample, the probe predominately experiences repulsive Van der Waals forces (contact mode). This leads to the tip deflection described previously. As the tip moves further away from the surface attractive Van der Waals forces are dominant (non-contact mode).

4 Piezoelectric Tube Scanner

Piezoelectric tube scanner (PTS) is an important feature of the AFM. The PTS is used as the positioning unit in the AFM. In most of the cases the PTS is usually fabricated from lead zirconium titanate, (PZT) by pressing together a powder, then sintering the material. The PTS is designed to achieve fine mechanical displacement in the x, y and z axis. Earlier before the invention of the PTS, the three dimensional positioning of the AFM was achieved by tripod scanner. But due to lateral bending, it causes cross coupling and low mechanical resonance which limit the scanning speed of the AFM. Later using the piezoelectricity technology, PTSs were made. The PTS works based on the theory of piezoelectric effect. About 100 years before

than the time of the invention of the STM, Curie brothers, Pierre Curie and Jacques Curie (1880) discovered the piezoelectric effect in the materials.

Piezoelectric materials are ceramics that change dimensions in response to an applied voltage and conversely, they develop an electrical potential in response to mechanical pressure. Piezoelectric materials are polycrystalline solids. Each of the crystals in a piezoelectric material has its own electric dipole moment. These dipole moments are responsible to move the piezo in response to an applied voltage. The dipole moments within the scanner are randomly aligned after sintering. The ability of the scanner to move depends on the align of the dipole. If the dipole moments are not aligned, the scanner has almost no ability to move. The align of the dipole moment is done by using a process called poling.

The process of poling in the scanner is done at 200 °C to free the dipoles. At this moment a direct current voltage source is applied. It takes few hours to align the dipoles. After the aligning process the scanner is cooled to freeze the dipoles into their aligned state. Then electrodes are attached to the outside of the tube, segmenting it electrically into vertical quarters, for $+x$, $+y$, $-x$, and $-y$ travel. The electrode in the z direction of the scanner is attached in the center of the scanner. A typical illustration of a PTS is presented in Fig. 4.

The PTS given in Fig. 4 shows that the PTS is typically consists of a cylindrical tube made of radially poled piezoelectric materials. The PTS is fixed at one end and free at other end. The PTS is segmented into four equal size electrodes. The electrodes are marked as +X, −X, +Y in the figure. Another electrode is not marked in the picture because the electrode is at the opposite end of the figure. The top part of the electrode is unsegmented. Usually a sample holder is placed on the top of the scanner to hold the sample.

Alternating voltages are applied to the $+x$ and $-x$ electrodes of the scanner. The application of this voltage induces strain into the tube which causes it to bend back and forth in the lateral, i.e. the x direction. Similar method is used to apply voltage in the y direction of the scanner. The expansion and contraction of the PTS depends on the polarity of the applied voltage with respect to the polling direction of the material. The PTS expands when the polarity of the applied voltage coincides with the polling direction. The PTS contracts when the the polarity of the applied voltage opposite with the polling direction. Voltages applied to the z electrode cause the scanner to extend or contract vertically. The displacement of the scanner is measured by using sensors. In most of the cases capacitive sensors are used to measure the displacement of the scanner. The reason for using capacitive sensors is their high speed response.

The maximum scan size of the PTS depends on many factors. This includes the length of the scanner tube, the diameter of the tube, its wall thickness, and the strain coefficients of the particular piezoelectric ceramic from which it is fabricated. Typically the PTS can scan from tens of angstroms to over 100 μ in the lateral and longitudinal direction. In the vertical direction it can scan from the sub-angstrom range to about 10 μ. One of the PTS used in this thesis is illustrated in Fig. 5. In this thesis we have used three scanners. We started our experiments with one scanner first. Then after the damage of first scanner we have used a second scanner and ordered a new scanner. Few works of this thesis is done using new scanner as well.

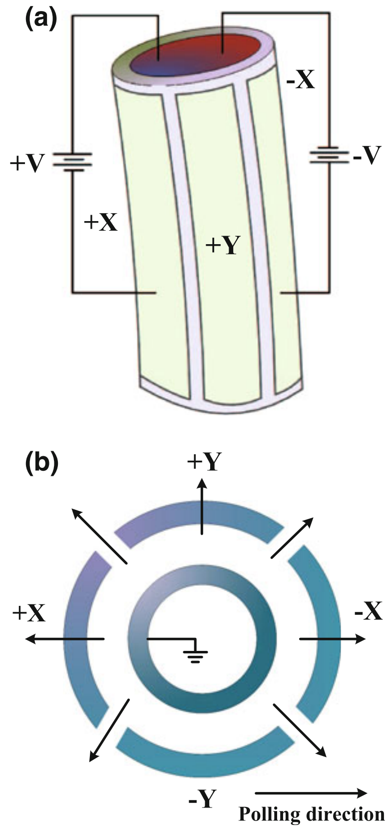

Fig. 4 A typical illustration of a piezoelectric tube scanner. **a** Side view and **b** top view

Fig. 5 A typical piezoelectric tube scanner

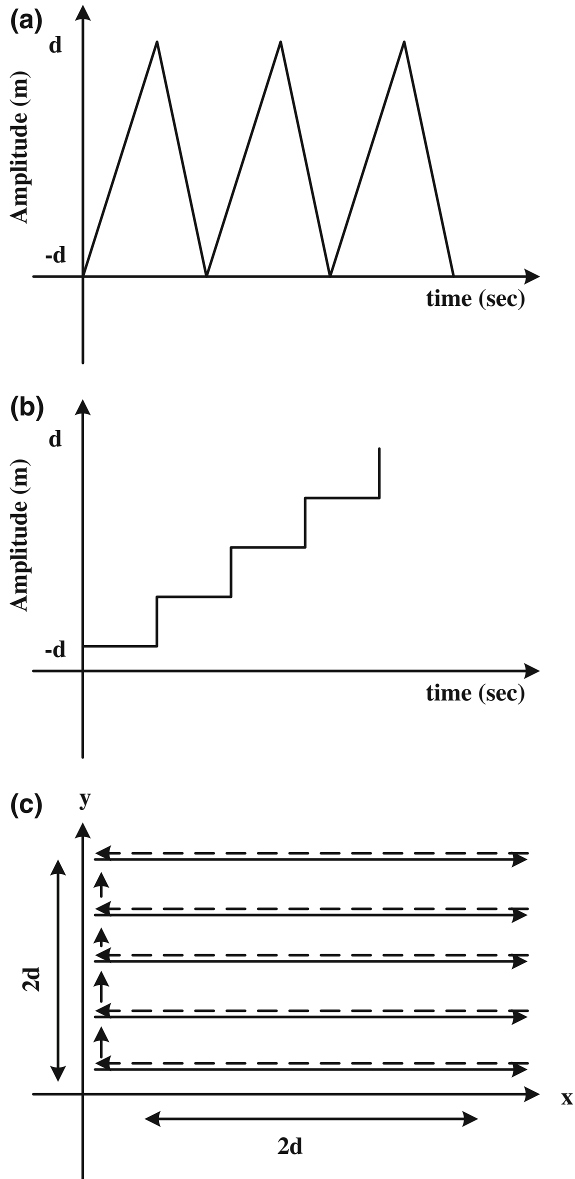

Fig. 6 Raster scanning method in AFM imaging. **a** Triangular signal uses in the *x*-axis, **b** staircase signal uses in the *y*-axis and **c** raster scanning method

In most of the cases the scanning operation in the AFM is performed by using raster scanning pattern. The raster scanning is performed by moving the PTS in forward and backward direction along the *x*-axis and moving the PTS in a small step in *y*-axis. This is done by applying triangular signal in the *x*-axis and staircase signal in the *y*-axis as shown in Fig. 6a, b. When the triangular signal is applied to *x*-axis and a staircase signal is applied to *y*-axis a raster scanning pattern is generated as shown in Fig. 6c.

5 Limiting Factors for High Speed Nanopositioning of the PTS

The imaging performance of the AFM often depends on the accurate positioning performance of the PTS. In order to achieve high quality images of the sample, accurate positioning of the PTS is required. The precision positioning of the PTS depends on the perfect tracking of the reference signals used in the AFM imaging. The high speed imaging performance of the AFM is limited due to some inherent properties of the PTS such as hysteresis, creep and induced vibration. In the following section these issues are further discussed.

5.1 Hysteresis

The term "hysteresis" is derived from an ancient Greek word "hustereia" meaning "deficiency" or "lagging behind". It was Sir James Alfred Ewing who describes the behavior of magnetic materials around 1890. Hysteresis is the dependence of a system which not only depends on its current environment but also on its past environment. This dependence arises because the system can be in more than one internal state. It is the lag in response exhibited by a body in reacting to changes in the forces.

Hysteresis can be represented graphically as a relation in the u–y plane. Figure 7 shows an example of an hysteresis relation along with a sample path. The loop

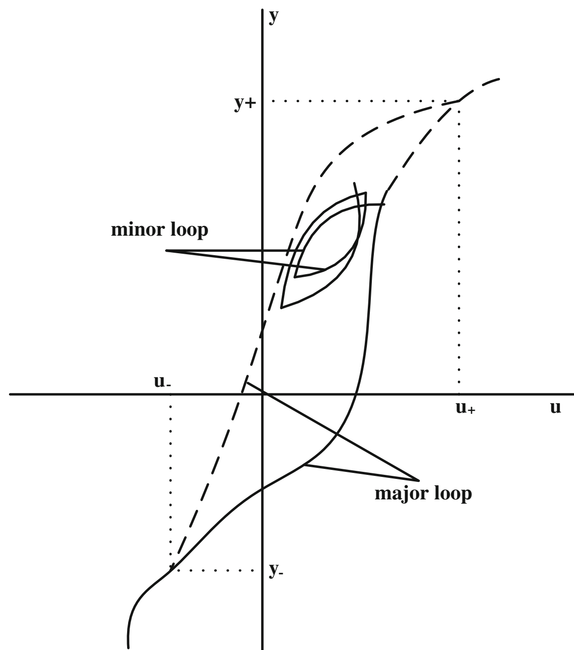

Fig. 7 Hysteresis terminology

which bounds the region where $y(t)$ is multi-valued is called major loop. The domain of input values u corresponding to this region is $[u_-, u_+]$; the range of outputs $[y_-, y_+]$. Each new segment of the output path in the u–y plane is called a branch. Successive branches which cross inside the major loop form minor loops.

Hysteresis arises in diverse applications such as magnetic hysteresis is a typical example. Hysteresis occurs in ferromagnetic materials and ferroelectric materials, as well as in the deformation of some materials (such as rubber bands and shape-memory alloys) in response to a varying force. The PTS is also fabricated from piezoelectric materials which are ferromagnetic in nature. The ferromagnetic nature of the PTS introduces hysteresis in the PTS. In most of the cases the PTS in the AFM is driven by a voltage source. This voltage source is responsible to introduce hysteresis in the PTS (Figs. 8 and 9).

The amount of the effect of the hysteresis in the PTS depends on the magnitude and frequency of the applied voltage signal. The effect of hysteresis increases with the increase of the magnitude and frequency of the applied voltage signal. Due to

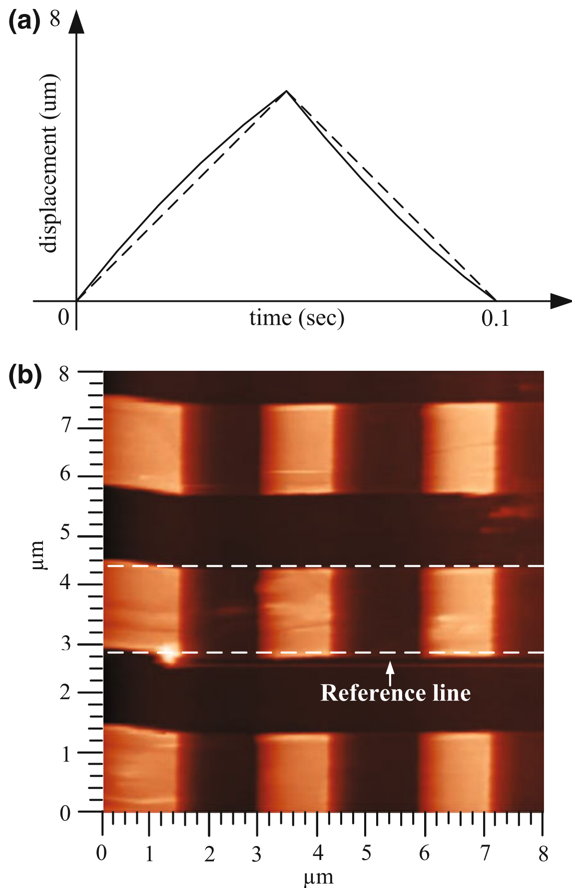

Fig. 8 Effect of hysteresis in imaging. **a** Measured scanners's displacements (*solid line*) for a 10 Hz triangular signal input (*dashed line*), **b** the resulting image of a calibration grating sample

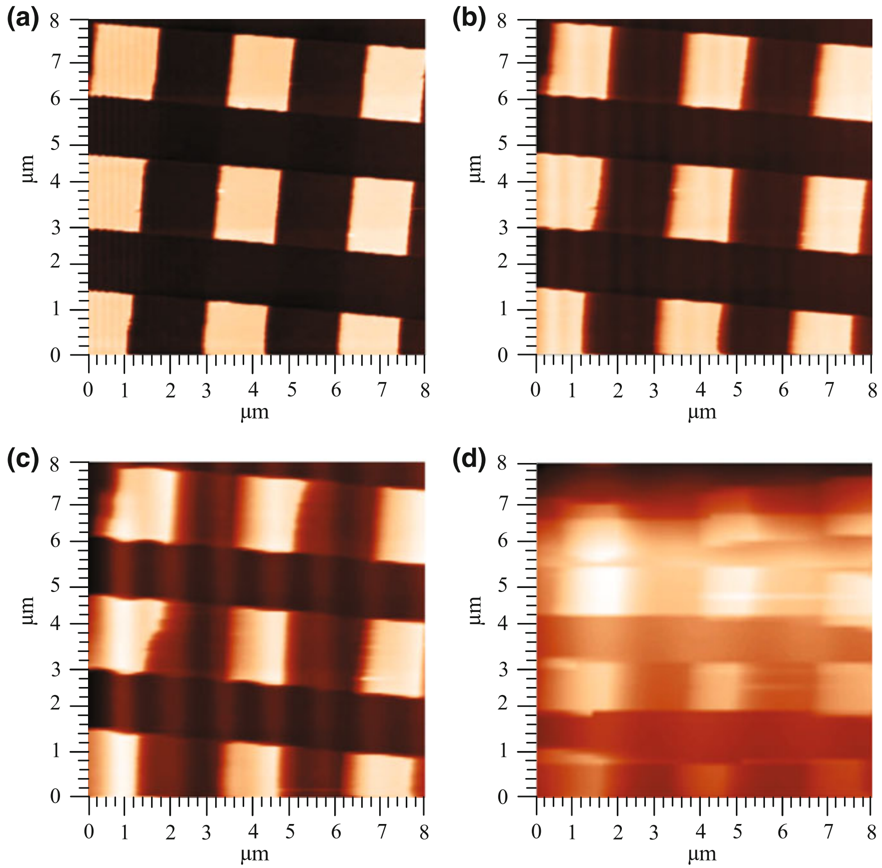

Fig. 9 Open-loop scanned images **a** 15.62 Hz **b** 31.25 Hz **c** 62.5 Hz **d** 125 Hz

the hysteresis effect distortion occurs in the scanned images of the AFM. As the fast axis of the PTS is driven by triangular signal, a deviation of 15 % can occur due to the hysteresis. This effect can be minimized by allowing scan only for low range. This limits the scanner ability for long range scan.

A number of researches available in the literature to model the hysteresis. The most commonly presented hysteresis models can be summarised as follows: Electromechanical models [1], Preisach models [35], Prandtl-Ishlinskii (PI) models [2], Bouc-Wem models [34], Rate-dependent or rate-independent hysteresis models [5]. The compensation of the effect of hysteresis is important because this effect tends to deviate the PTS from accurate nanopositioning. One way to compensate for hysteresis is to model it as a nonlinear function and then eliminate it by cascading its inverse with piezoelectric tube actuator. Though it is useful for open-loop but it requires accurate modeling of the system to compensate hysteresis as it may change with the parameter variation. Current and charge sources can also be used to reduce

the hysteresis instead of voltage source. One of the disadvantages of using the charge source is that, it leads to drift and saturation problem which greatly reduce the range of piezoactuators.

Feedback control technique has also been applied to reduce the hysteresis. Integral or proportional integral (PI) controllers are used in most AFM systems because of their simplicity and ease of implementation. Another advantage of the use of the integral or PI controllers is that these controllers apply high gain at low frequency. This high gain of the integral controller results in reduction of the effect of hysteresis.

5.2 Creep

Piezoelectric creep effect is another major constrain for high speed nanopositioning of the PTS. The creep effect is mainly prominent at slow scanning rate. The creep effect distorts the generated images from the AFM. When a voltage signal is applied across the PTS to move the piezo in three direction, the piezo continuous to displace even after the removal of the induced voltage. This generates the creep effect in the PTS. The creep effect can be minimized by allowing sufficient amount of time.

5.3 Induced Vibration

The X axis of the PTS is actuated by using a triangular signal. The triangular signal contains all odd harmonics of its fundamental frequency. When the PTS is actuated using triangular signal, the odd harmonics of the triangular signal excite the mechanical resonant mode of the PTS. This hampers the tracking accuracy of the PTS. The effect of the induced vibration in AFM imaging is presented in Fig. 25. The comparison shows that the generated images are more distorted at high frequencies as compared to the low scanning speeds.

6 Background

Different approaches [4, 10, 50, 51, 54, 55] to improve the tracking accuracy of nanopositioners can be categorized into two groups, (a) open-loop and (b) closed-loop control. The open-loop control techniques [16] are of interest as they are capable of providing a bandwidth close to the first resonance mode of scanners. The performance of the open-loop control technique depends on accurate system modelling. Two types of nanopositioners are used in SPM systems (a) scan-by-sample and (b) scan-by-head. The dynamics of scan-by-sample scanners change due to the

load change and the dynamics of scan-by-head nanopositioners change due to environmental factors such as outside temperature and humidity.

Feedback-linearized inverse feed-forward methods [36] are designed for reducing vibration in a scanner. The inversion technique can provide a closed-loop bandwidth near or greater than the resonance frequency if the resonance frequency of the PTS remains fixed. The resonance frequency of the scanner does not remain fixed but rather changes with the changing loads on the scanner. A high gain inversion-based feedback controller can make the closed-loop system unstable if the resonance frequency of the scanner changes.

Feedback controllers can provide robustness against the changes in the dynamics of the plant [10, 17–22, 50, 51, 54]. Most commercial SPM systems use integral or proportional integral (PI) controllers because of their simplicity and ease of implementation. One of the drawbacks of using integral controllers in nanopositioning applications is the loss of performance with the changes in plant dynamics. The bandwidth of integral controllers for nanopositioners is limited to $2\omega\xi$, where ω and ξ are the first resonance frequency and damping constant of nanopositioners [26].

Negative imaginary (NI) controllers [46] such as resonant controllers [22], positive position feedback (PPF) controllers [39], integral resonant controllers (IRCs) [29] are designed to improve the tracking performance of integral controllers for nanopositioners. By definition NI systems are stable systems with an equal number of inputs and outputs. A transfer function $G(s)$ is said to be NI if $j[G(j\omega) - G^*(j\omega)] \geq 0$ for all $\omega \in (0, \infty)$ [45]. For a SISO NI system $G(s)$, this is equivalent to the phase condition $\angle G(j\omega) \in [-\pi, 0]$ for all $\omega \in (0, \infty)$ [46]. The positive feedback interconnection between two NI systems $M_1(s)$ and $M_2(s)$ is stable if $|M_1(0)||M_2(0)| < 1$ and one of the system is strictly NI. A transfer function $G(s)$ is said to be strictly negative-imaginary if $j[G(j\omega) - G^*(j\omega)] > 0$ for all $\omega \in (0, \infty)$ [45].

The improvement in performance of nanopostioners using integral controllers is achieved by providing additional damping to the resonant modes of nanopositioners. The motivation to use NI damping controllers to improve the tracking performance of integral controllers is their robustness against the changes in plant dynamics [29]. The IRCs and PPF controllers are low pass controllers. The closed-loop system between scanners and the IRCs and PPF controllers may result in low gain and phase margin due to the low pass nature of the controllers. The resonant controllers are known for providing excellent damping of resonant modes of scanners with large gain and phase margin due to their high pass nature [47]. The high pass nature of resonant controllers may result in high frequency sensor noise which limits the use of the resonant controllers for PTSs.

Passive damping controller such as velocity feedback controllers [6] are also designed to damp the first resonant mode of the scanner. A linear system $P(s)$ is said to be passive if $\mathrm{Re}[P(j\omega)] \geq 0$ for all $\omega > (0, \infty)$ [45]. If a square transfer function matrix $P(s)$ is passive then it follows that $P(j\omega) + P^*(j\omega) \geq 0$, for all $\omega \in \mathbb{R}$ such that $s = j\omega$ is not a pole of $P(s)$ [46] where $P^*(j\omega)$ is the complex conjugate transpose of the matrix $P(j\omega)$. If $P(s)$ is a single-input single-output (SISO) passive transfer function, then, this is equivalent to the phase condition $\angle P(j\omega) \in [-\pi/2, \pi/2]$ for all $\omega > (0, \infty)$. The motivations to design passive damping

controllers for piezo scanners are their band pass nature and robustness against the changes in plant dynamics. The bandpass nature of the passive damping controller for piezo scanner results in large gain and phase margin.

Passive and NI systems are of interest because of their many practical applications, e.g., lightly damped flexible structures with collocated velocity sensors and force actuators [6, 46] and collocated position sensors and force actuators. The term collocated refers to the fact that the sensors and the actuators have the same location and same direction [48]. A guarantee of the closed-loop stability between systems with collocated velocity sensors and force actuators and passive controllers can be established using the passivity theorem [6].

However, in practice the transfer function matrix between the force actuators and position sensors of piezo scanners is neither NI nor passive [45]. Possible reasons for the PTS system not being NI or passive are delays in the sensor or actuator electronics or the collocation of the sensors and actuators may not be perfect. The electronic systems to which a PTS is connected can also add additional phase lag to the system. Therefore the finite-gain stability between the NI and passive damping controllers and piezo scanner can not be established by using NI and passivity theorem alone. A survey of control issues relating to damping based controllers for nanopositioners can be found in [23].

Some previous approaches to the design of damping controllers for piezoelectric tube scanners are based on a single-input single-output (SISO) approach [10, 11]. The axes of the PTSs are considered as independent decoupled single-input single-output systems. In practice, the axes of the nanopositioners are not independent SISO systems. There exists a strong cross coupling effect [25] between the lateral and longitudinal axes of the piezo scanner. Therefore, the design of the SISO controller for piezo scanners cannot guarantee the closed-loop stability.

Model based controllers such as H_∞ [52, 56, 57, 59, 60] controllers are designed for improving the damping and tracking performance of the scanner based on a SISO approach. The design methodology proposed in [52, 56, 59, 60] ignores the effect of cross coupling in the piezoelectric tube scanner.

The cross coupling [25] between the axes of the nanopositioner introduces a significant amount of error for high speed precision positioning. Due to the cross coupling effects the signal applied to one of the axes of the nanopositioner results in a displacement in both axes of the nanopositioner which affects the accuracy of the piezo scanners and if the magnitude of the cross coupling effect is high then the resulting images generated from AFMs are tilted as shown in Fig. 10.

New types of non-raster scanning methods such as spiral scanning [32], cycloid scanning [65], and Lissajous scanning [62] are proposed as alternatives to raster scanning for fast image scanning. The positioning accuracy for spiral scanning, cycloid scanning, and Lissajous scanning is limited due to the presence of cross coupling effects between the axes of scanners.

Design of multi-variable controllers for piezo scanner is of interest because of their ability to consider both the bandwidth and the cross coupling effect in the design process. A SISO damping based controller [29] achieves a bandwidth near to the first resonance frequency of the scanner with no guarantee of the reduction of

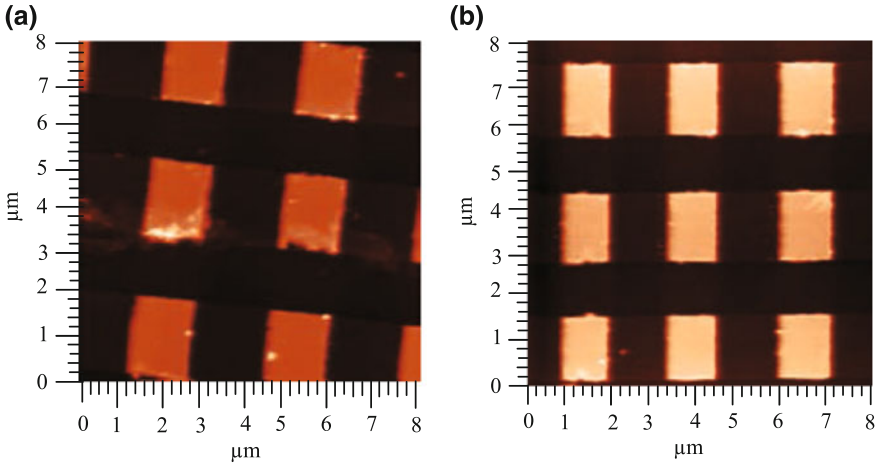

Fig. 10 Effect of cross coupling in surface imaging **a** scanned image with more cross coupling effect and **b** scanned image with less cross coupling effect

cross coupling effects between the axes of scanners. The SISO controller design has no provision to attenuate the cross coupling effects, while a MIMO controller gives a direct way to consider both the bandwidth and cross coupling effects between the axes of scanners.

A MIMO integral resonant controller is implemented [9] to speed up the performance of the AFM by considering the cross coupling effects in the lateral and longitudinal axis of the PTS as symmetric. The MIMO integral resonant controller (IRC) [9] was designed only to achieve maximum bandwidth. The design methodology of IRC [9] does not guarantee the reduction of the cross coupling effect between the axes of the PTS. Also, the IRC controller does not result in zero steady state error which in turn limit the ability of the IRCs to reduce the effect of nonlinearities in the form of hysteresis.

Minimizing the effect of hysteresis is one of the another challenge in designing tracking controller for atomic force microscopes. The tracking performance of PTS is largely affected due to the effect of hysteresis. A deviation of 15 % can occur between the forward and backward movements of the applied signal due to the effects of hysteresis [29, 39]. Integral controllers are designed because of their ability to compensate the effect of hysteresis. The high gain of the integral controller forces the system to track. This reduces the effect of hysteresis at low frequencies. Although the use of integral controller reduces the effect of hysteresis, however, a great challenge with the integral controller is their low closed-loop bandwidth. Current and charge sources [28] can be possible solution instead of voltage sources to reduce the effect of hysteresis in the PTSs. A fivefold reduction in the effects of hysteresis can be achieved using a charge source instead of a voltage source [10, 11]. However, the use of charge sources to drive piezo scanners introduces saturation problems.

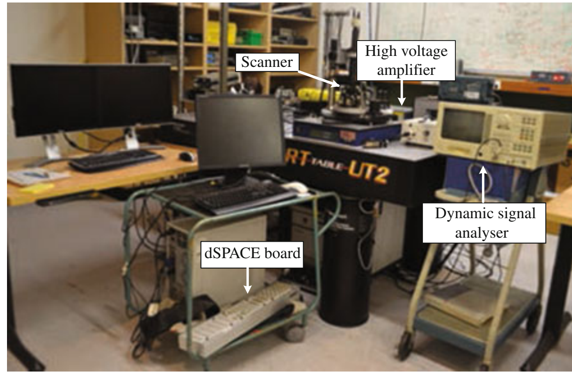

Fig. 11 Experimental setup used in the present work

7 Experimental Setup

The experimental setup consists of (i) an NT-MDT Ntegra scanning probe microscope which is configured to operate as an AFM, (ii) a piezoelectric tube scanner (PTS) which works as a nanopositioner in this paper, (iii) a dynamic signal analyzer (DSA) to measure the frequency response of the PTS at various frequencies of sinusoid signals, (iv) a high voltage amplifier (HVA) with a gain of 15 to apply voltage to the PTS, (v) a signal access module (SAM) to allow direct access to the electrodes of the scanner, and (vi) a dSPACE board for implementing the controller on the nanopositioner as shown in Fig. 11. The experiments are performed at the University of New South Wales, Canberra, Australia.

8 System Identification

The controller design in this paper is based on the input-output data, i.e. the transfer function between the input and output only. The present work uses an experimental approach [27, 28, 39] to obtain a transfer function for the MIMO PTS lateral and longitudinal positioning system.

The transfer function of the MIMO PTS positioning system can be described by the following equation:

$$G(s) = [D_x, D_y]^T [\frac{1}{V_x}, \frac{1}{V_y}] \tag{1}$$

where $D_x(s)$ and $D_y(s)$ is the Laplace transform of the output voltage from the X and Y sensor attached with the PTS and $V_x(s)$ and $D_y(s)$ is the Laplace transform of the input voltage to the HVA for driving X and Y-axis of the piezo.

The above transfer function matrix in (1) has a state space realization of the following form:

$$\begin{aligned}\dot{x}(t) &= Ax(t) + Bu(t)\\ y(t) &= Cx(t) + Du(t)\end{aligned} \tag{2}$$

where u is the vector of the inputs to the HVA and y is the vector of the outputs from sensors.

Swept sine inputs of 100 mV rms were applied to the HVA to drive the piezoelectric scanner along the X and Y-axes from the dual channel DSA and the corresponding capacitive sensor responses were recorded. The following values of the A, B, C and D matrices of the above state space model are obtained by using the subspace based system identification method [42]:

$$A = \begin{bmatrix} -427.6 & -5583.6 & -1521.1 & 840.01 & -874.82 & 1074 \\ 4963.2 & -423.76 & -1040.6 & -1245.1 & -1828.2 & 1693.9 \\ 959.85 & 1010.9 & -690.68 & 5435.9 & 474.96 & 1528 \\ -587.17 & 1161.8 & -4395.2 & -508.85 & -2304.2 & -2166.5 \\ -102.38 & 609.98 & 458.09 & 1351.9 & -946.65 & 149.69 \\ 251.11 & -708.42 & 71.644 & 1020.2 & -8.7797 & -1686.1 \end{bmatrix},$$

$$B = \begin{bmatrix} 1.6893 & 12.168 \\ 12.022 & 10.622 \\ -0.42926 & 2.964 \\ 8.0813 & -10.904 \\ -17.019 & 1.1707 \\ 0.58665 & 18.898 \end{bmatrix},$$

$$C = \begin{bmatrix} 9.0521 & 16.8150 & -27.5329 & 20.7708 & 35.2925 & 2.4245 \\ 25.6510 & 19.0371 & 30.2869 & -16.1956 & 6.4775 & -58.5076 \end{bmatrix},$$

$$D = \begin{bmatrix} 0 & 0 \\ 0 & 0 \end{bmatrix}.$$

The MIMO system identification process is done to capture first resonant mode of the PTS with low order model and the matching between the MIMO measured data and the identified model is given in Fig. 12. The MIMO identified model captures the first resonant mode of the measured MIMO data. The phase responses of the MIMO identified model is matched with the phases of the MIMO measured data at low frequencies whereas at high frequencies there is a slight difference between the phases of the measured data and the identified model.

The order of the identified model can be separated as follows: The first four orders of the identified model are used to capture the first resonant mode of the scanner in the X- and Y-axis and the rest of the orders of the identified model are representing all other dynamics of the system including delays.

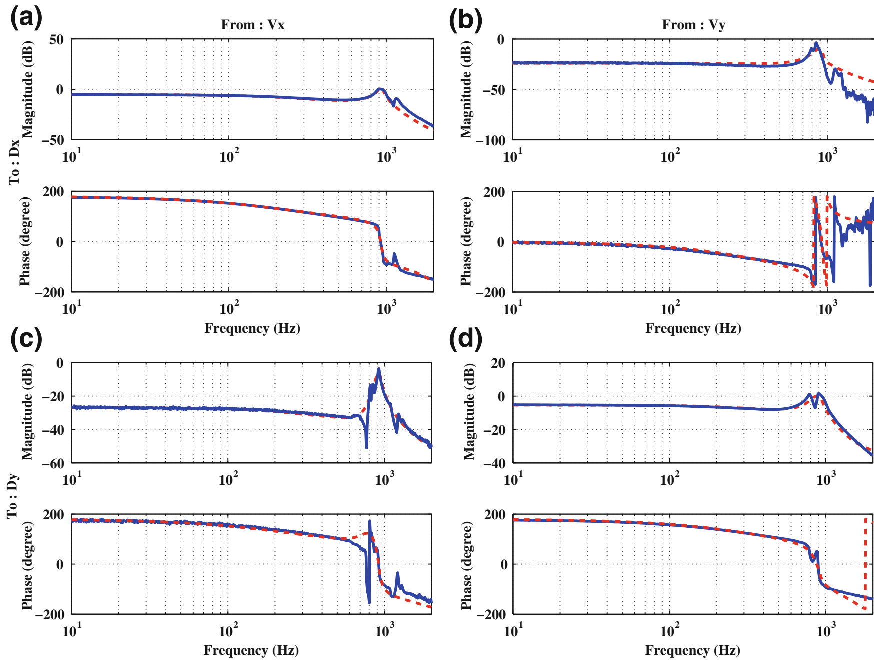

Fig. 12 Open-loop frequency response relating the inputs $[V_x, V_y]^T$ and the outputs $[D_x, D_y]^T$. The *solid line* (–) represents the measured frequency response and the *dashed line* (- -) represents the identified model frequency response. **a** Magnitude frequency response from Vx to Dx, **b** magnitude frequency response from Vy to Dx, **c** magnitude frequency response from Vx to Dy, and **d** magnitude frequency response from Vy to Dx

9 Controller Design

As previously discussed, the PTS suffers from the problem of low mechanical resonance frequency, the first step of this work is to suppress the first resonant mode of the PTS. In order to damp the first resonant mode of the PTS, a MIMO passive damping controller is designed. This type controller is of interest because of its ability to avoid closed-loop instability due to the spill over effect of PTS at high frequencies [6]. The block diagram of the closed-loop system for damping the first resonant mode by using passive damping controller is given in Fig. 13 where $G(s)$ is the plant transfer function matrix, $H_{FB}(s)$ is the transfer function matrix of the passive damping controller, u_1, u_2 are reference signals and y_1, y_2 are sensor output signals. The transfer function matrix of the MIMO passive damping controller is as follows:

$$H_{FB}(s) = -\frac{k_v s}{s^2 + 2\xi_v \omega_v s + \omega_v^2} \beta_{m\times m} \quad (3)$$

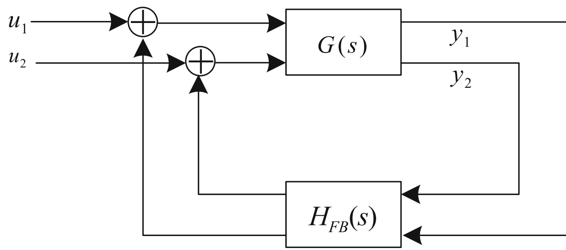

Fig. 13 Block diagram of the closed-loop system for first resonant mode damping of the PTS

where $k_v > 0$ is the gain of the controller, $\xi_v > 0$ and $\omega_v > 0$ are the damping constant and the frequency at which resonant mode needs to be damped. $\beta_{m\times m}$ is a matrix of order $m \times m$. Here, m is the number of inputs and the number of outputs of the system. For the PTS $\beta_{m\times m}$ is a 2×2 matrix.

The piezoelectric tube scanner used in this paper is a system with "mixed" negative-imaginary and small-gain properties Patra and Lanzon [44]. A system having "mixed" negative-imaginary and small-gain properties shows NI property [45] for some frequency range and small-gain property Patra and Lanzon [44] for other frequency range. The small-gain theorem states that, the feedback interconnection of two linear stable time invariant systems is stable if the product of the gains of the systems at each frequency is strictly less than one [38]. The design of the damping controller to damp the first resonant mode of the scanner in this paper is based on the mixed negative-imaginary and small-gain approach Patra and Lanzon [44].

The results of the "mixed" negative-imaginary and small-gain approach Patra and Lanzon [44] show that, the positive feedback interconnection as given in Fig. 13 between two strictly proper, causal and linear time invariant systems $G(s)$ and $H_{FB}(s)$ with mixed negative-imaginary and finite-gain properties bounded by gains k_1 and k_2, respectively is stable if the following conditions are satisfied:

(1) $\lim_{\omega\to\infty} G(j\omega)H_{FB}(j\omega) = 0$.
(2) The systems $G(s)$ and $H_{FB}(s)$ are bounded by gains k_1 and k_2, respectively such that, $k_1 > |G(0)|$, $k_2 > |H_{FB}(0)|$, and $k_1k_2 < 1$.
(3) In the intervals, $\omega \in [\omega_i, \omega_{i+1}]$, for $i = 1, 2, \ldots$, where $G(j\omega)$ does not have the NI property, both $G(j\omega)$ and $H_{FB}(j\omega)$ must be bounded by gains k_1 and k_2, i.e. $|G(j\omega)| < k_1$ and $|H_{FB}(j\omega)| < k_2$ for all $\omega \in [\omega_i, \omega_{i+1}]$, for $i = 1, 2, \ldots$.
(4) In the intervals, $\omega \in [\omega_p, \omega_{p+1}]$, for $p = 1, 2, \ldots$, where $G(j\omega)$ has the NI property and bounded by the gain k_1, $H_{FB}(j\omega)$ must either have NI property or be bounded by the gain k_2 or both.

In order to translate the mixed negative-imaginary and small-gain approach into a suitable design process for the piezoelectric tube scanner and the damping controller the following steps are carried out:

(i) Find the frequencies at which the system $G(s)$ has the NI property.
(ii) Select a gain k_1 such that at the frequencies where $G(s)$ does not have the NI property bounded by the gain k_1.
(iii) Make the gain k_1 as low as possible such that, $G(s)$ has either the NI property or has a finite-gain bounded by the gain k_1 or both at each frequency in order to achieve a large gain of the controller.
(iv) Find the frequencies at which $G(s)$ has only the NI property, only the finite-gain property bounded by the gain k_1 and both.
(v) Select the controller $H_{FB}(s)$ parameters and find the frequencies at which $H_{FB}(s)$ has the NI property.
(vi) Increase the gain of the controller $H_{FB}(s)$ to be as large as possible and select the gain k_2 for $H_{FB}(s)$ such that, (a) $k_1 k_2 < 1$, (b) $H_{FB}(s)$ has only the NI property at the frequencies where $G(s)$ has only the NI property, (c) $H_{FB}(s)$ has only the finite-gain property bounded by the gain k_2 at the frequencies where $G(s)$ has only the finite-gain property bounded by the gain k_1, and (d) $H_{FB}(s)$ has either the NI or finite-gain properties bounded by k_2 at the frequencies where $G(s)$ has both the NI and finite-gain properties bounded by the gain k_1.

The values of the $H_{FB}(s)$ parameters obtained in the designed process is as follows: $\omega_v = 925.8021\,\text{Hz},\ \xi_v = 0.56,\ k_v = 7000$, and $\beta_{m\times m} = \begin{bmatrix} 0.66 & 0.005 \\ 0.005 & 0.66 \end{bmatrix}$.

9.1 Stability Analysis of the Interconnected System

The MIMO damping controller design is based on the maximum singular value of the plant $G(s)$ and the controller $H_{FB}(s)$. The maximum singular value plot of $G(s)$ and $H_{FB}(s)$ for positive frequencies are shown in Figs. 14 and 15, respectively. Selecting $k_1 = 1.37(> \bar{\sigma}(G(0)) = 0.5519)$ and $k_2 = 0.725(> \bar{\sigma}(H_{FB}(0)) = 0.0)$ respectively, the mixed properties between $G(s)$ and $H_{FB}(s)$ is shown in Fig. 16. One could also select different bounds so that, $k_1 > \bar{\sigma}(G(0))$ and $k_2 > \bar{\sigma}(H_{FB}(0))$ and the condition $k_1 k_2 < 1$ is satisfied.

$G(s)$ has only the small-gain properties between 0 and 5817 rad/s and between 1.0638×10^4 rad/s and ∞. $G(s)$ has both small-gain and the negative-imaginary properties between $5,817$ rad/s and 1.0638×10^4 rad/s. $H_{FB}(s)$ has both negative-imaginary and small-gain properties between 0 to 5,817 rad/s and after that $H_{FB}(s)$ does not show the negative-imaginary properties. It can be seen that, at each frequency when $G(s)$ has the NI property, $H_{FB}(s)$ also has the NI property; and when $G(s)$ has the finite-gain property bounded by gain k_1, $H_{FB}(s)$ has the finite-gain property bounded by gain k_2 and $k_1 k_2 < 1$. Hence, the closed-loop system corresponding to interconnection between $G(s)$ and $H_{FB}(s)$ is stable. Therefore, the conditions of Theorem 1 “mixed” negative-imaginary and small-gain approach Patra and Lanzon [44] are satisfied.

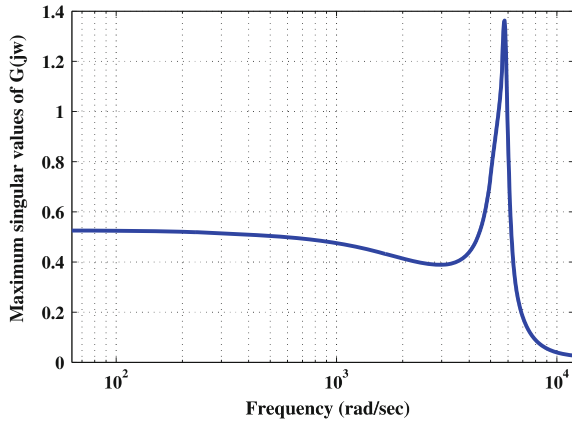

Fig. 14 Maximum singular value $(\bar{\sigma}(G(j\omega)))$ plot of $G(s)$

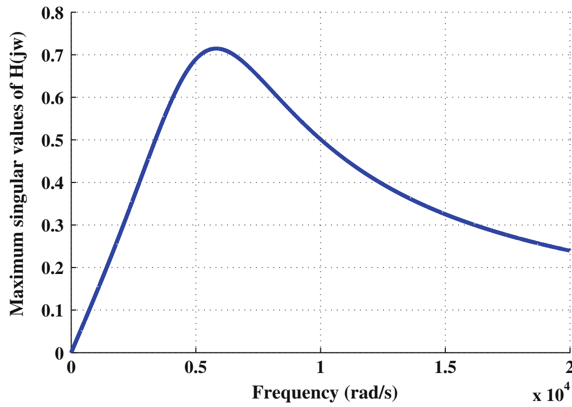

Fig. 15 Maximum singular value $(\bar{\sigma}(H(j\omega)))$ plot of $H_{FB}(s)$

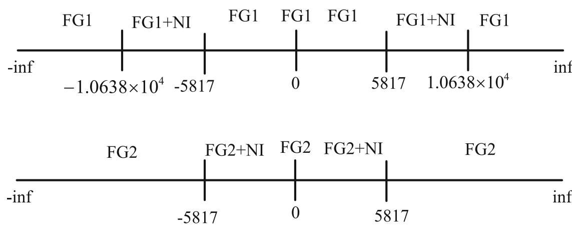

Fig. 16 Frequency intervals (*NI* negative imaginary, *FG1* finite-gain for system *G*, *FG2* finite-gain for system H_{FB})

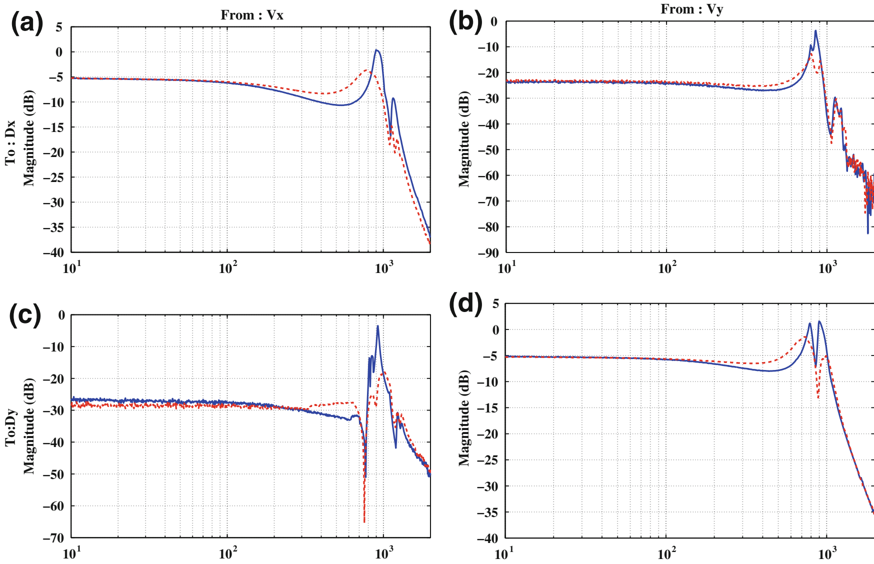

Fig. 17 Comparison of the magnitude frequency response relating the inputs $[V_x, V_y]^T$ and the outputs $[D_x, D_y]^T$. The *solid line* (–) represents the measured open-loop frequency response and the *dashed line* (- -) represents the measured closed-loop frequency response. **a** Magnitude frequency response from V_x to D_x, **b** magnitude frequency response from Vy to Dx, **c** magnitude frequency response from Vx to Dy, and **d** magnitude frequency response from Vy to Dx

The performance of the damping controller is examined by implementing the damping controller on an NT-MDT scan by sample piezoelectric tube scanner. The comparisons of the open- and closed-loop frequency responses by implementing the MIMO damping controller given in Fig. 17 show that the MIMO damping controller is able to provide 3.5 damping of the first resonant mode in the diagonal axes of the PTS.

9.2 Design of a Controller for Damping, Tracking and Cross Coupling Attenuation

The damping controller $H_{FB}(s)$ applied in the feedback path is able to provide a 3.5 damping of the first resonant mode in the diagonal axes of the PTS. Due to the low gain at low frequencies $H_{FB}(s)$ does not able to track the reference signal. In order to track the reference signal a high gain integral controller $C_{FF}(s) = \frac{k_i}{s}\alpha_{m\times m}$, where k_i is the gain of the integral controller and $\alpha_{m\times m}$ is matrix of order $m \times m$ is added in the feed-forward path of the closed-loop system as shown in Fig. 18.

The values of the parameters of the integral controller for the scheme shown in Fig. 18 is obtained to follow a reference transfer function. The values of the

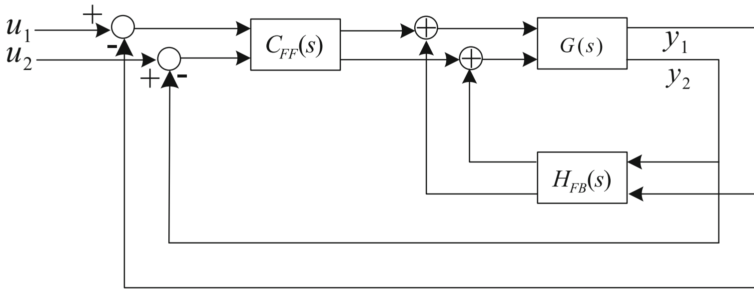

Fig. 18 Block diagram of the closed-loop system for resonant mode damping and tracking improvement

controller parameters are selected by minimizing H_2 norm of the difference between the reference and the actual closed-loop transfer function. The desired or the reference closed-loop transfer function is selected according to the aim of the design process, e.g., to achieve a desired bandwidth with small-cross coupling effects between the axes of the PTS. The desired closed-loop bandwidth is chosen from the observation of the system frequency response. The PTS used in this paper has its first resonant frequency at 918.3 Hz and after the first resonance frequency system rolls-off. It is expected the maximum bandwidth that can be achieved in the design is about 918.3 Hz. A closed-loop bandwidth higher than 918.3 Hz would require a high control input signals at high frequencies which in turn will increase the chances of adding high frequency noise signals.

The transfer function of the desired closed-loop system is chosen as

$$T(s) = \frac{1}{\tau s + 1} \begin{bmatrix} 1 & 0 \\ 0 & 1 \end{bmatrix} \tag{4}$$

where τ is selected to achieve desired bandwidth. In the present work τ is selected as $\frac{1}{918.3\,\mathrm{Hz}}$. The off-diagonal terms of $T(s)$ is zero which indicates that the aim of this MIMO controller design is to make the axes of the PTS independent. The transfer function of the actual closed-loop system of Fig. 18 is

$$T_{cl}(s) = \frac{G(s)C_{FF}(s)}{1 + G(s)(C_{FF}(s) - H_{FB}(s))}$$

The H_2 norm of the error transfer function between the desired $T(s)$ and the actual $T_{cl}(s)$ closed-loop transfer function is $\|E(s)\|_2 = \|T(s) - T_{cl}(s)\|_2$. A finite value of $\|E(s)\|_2$ guarantees the stability of the closed-loop system [19, 38]. The optimization was carried out by using simulated annealing algorithm. The optimization process took 5–8 min to obtain the values of the controller parameters. In the optimization process the initial values of the controller parameters are important for the convergence of the optimization.

In order to select the initial value of the parameters of the integral controller a single-input single-output (SISO) controller designed is performed first by considering each axis of the PTS as independent axis. The design of the SISO integral controller is done by using a root locus method. The initial values of the gain k_i and $\alpha_{m\times m}$ of the integral controller in the optimization process is selected $-1{,}000$ and $\begin{bmatrix} 1 & 0 \\ 0 & 1 \end{bmatrix}$. The maximum and minimum values of the controller parameters are also selected from the SISO design. The maximum value of the gain k_i and $\alpha_{m\times m}$ are selected as -800 and $\begin{bmatrix} 1.5 & 0.5 \\ 0.5 & 1.5 \end{bmatrix}$ and the minimum value of the gain k_i and $\alpha_{m\times m}$ are selected as $-1{,}800$ and $\begin{bmatrix} 0.5 & -0.1 \\ -0.1 & 0.5 \end{bmatrix}$. The convergence time of the optimization process depends on the difference between the minimum and maximum values of the parameters. The integral controller parameters achieved from the optimization process is $k_i = -1388.3$, $\alpha = \begin{bmatrix} 0.86 & 0.075 \\ -0.0587 & 1.15 \end{bmatrix}$.

At this point, it is straight forward to mention that the values of the controller parameters obtained in the optimization process are not for the global minimums of the objective function $\|E(s)\|_2$. A comparison of the open- and closed-loop magnitude frequency responses (MFRs) in the X and Y-axes of the PTS by implementing MIMO controller of the scheme of Fig. 18 is given in Fig. 19. The comparisons of the MFRs show that the closed-loop bandwidth achieved by the scheme of Fig. 18 is only 150 and 220 Hz in the X- and Y-axis of the scanner. The damping achieved by the proposed controller is 20 dB in the both axes of the PTS whereas the damping achieved by the integral controller is only 5 dB.

The MIMO integral controller was added with the MIMO damping controller as shown in Fig. 18 to improve the closed-loop tracking performance at low frequencies. However, due to the low gain of the integral controller at high frequencies, the resultant closed-loop system of Fig. 18 is only able to achieve a bandwidth of 150 and 220 Hz in the X- and Y-axis of the scanner which is still not high enough for the high speed nano-positioning of the PTS. Now, in order to increase the gain of the integral controller at high frequencies a high pass NI damping controller namely the resonant controller $H_{FB}(s)$ is added with the integral controller as shown in Fig. 20. The resonant controller is a high pass controller and adds gain where gain is lower due to the integral controller which in turns increase the bandwidth of the closed-loop system, whereas the other damping controllers such as the integral resonant controller or PPF controller are low pass in nature. The transfer function matrix of the resonant controller $H_{FF}(s)$ used in this paper has the following form:

$$H_{FF}(s) = \frac{s^2 + 2\xi_{\mathrm{ff}}\omega_{\mathrm{ff}}s}{s^2 + 2\xi_{\mathrm{ff}}\omega_{\mathrm{ff}}s + \omega_{\mathrm{ff}}^2}\Omega_{m\times m} \tag{5}$$

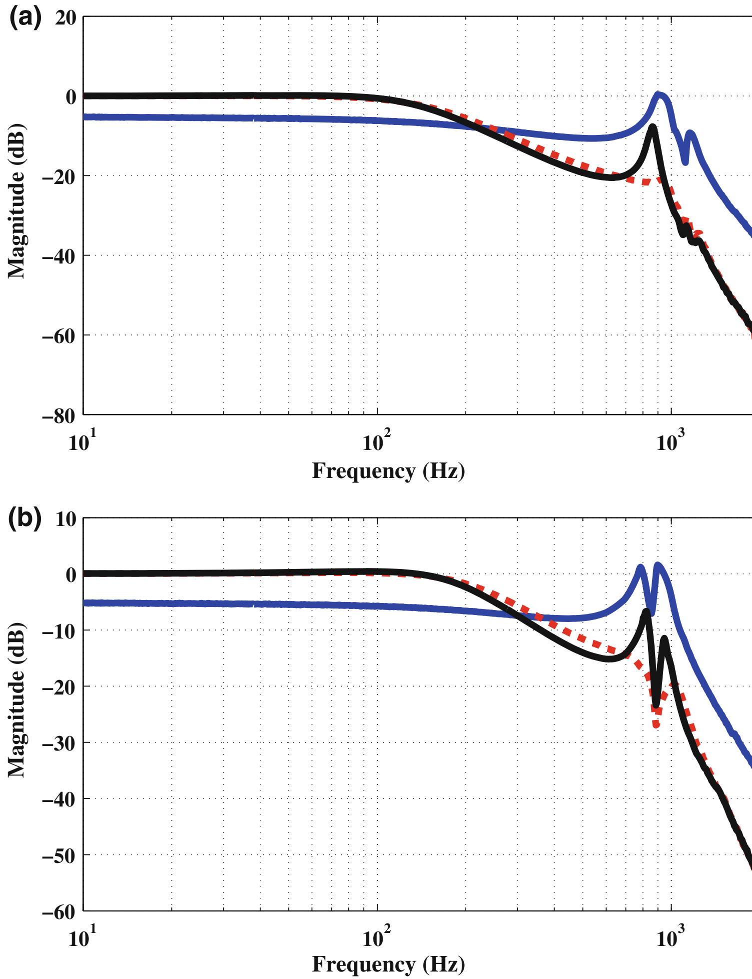

Fig. 19 Comparisons of the open- (the *blue solid line*) and closed-loop magnitude frequency responses obtained by using the MIMO integral controller (the black solid line) and the MIMO integral controller with MIMO damping controller (the *red dashed line*) in the X-axis (**a**) and Y-axis (**b**) of the scanner

where ξ_{ff} is the damping constant, ω_{ff} is the resonance frequency, and $\Omega_{m \times m}$ is a matrix of order $m \times m$. The resonant controller has a zero at the origin in its transfer function which means that the gain of the resonant controller at low frequencies is low. The value of ω_{ff} indicates the frequency where the gain of the resonant controller is maximum. Since the resonant controller is used only to increase the

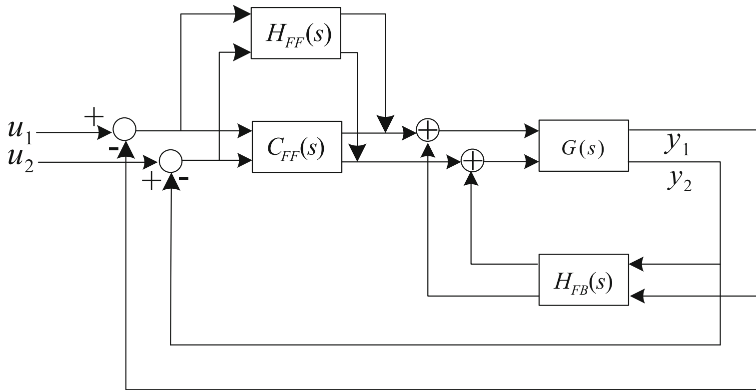

Fig. 20 Block diagram of the closed-loop system for resonant mode damping, tracking and bandwidth improvement

bandwidth, the damping constant ξ_{ff} should be high. A low value of damping constant ξ_{ff} introduces a notch and undesirable phase shift in the closed-loop.

The transfer function of the actual closed-loop system of Fig. 20 is

$$T_{close}(s) = \frac{G(s)(C_{FF}(s) + H_{FF}(s))}{1 + G(s)(C_{FF}(s) + H_{FF}(s) - H_{FB}(s))}$$

The values of the parameters of the integral controller and the resonant controller for the scheme of Fig. 20 are also obtained by minimizing H_2 norm of the difference between the desired $T(s)$ and the actual $T_{close}(s)$ closed-loop transfer functions. In a similar way discussed above, an optimization process by using simulated annealing algorithm is carried out to minimize $\|E(s)_{close}\|_2 = \|T(s) - T_{close}(s)\|_2$. The values of the integral controller and the resonant controller parameters obtained from the optimization process are as follows: $k_i = -1403.6$, $\alpha = \begin{bmatrix} 0.9 & 0.097 \\ -0.097 & 1.1 \end{bmatrix}$, $\xi_{ff} = 0.7$, $\omega_{ff} = 7,800$, $\Omega_{m\times m} = \begin{bmatrix} 1.8 & 0.1 \\ 0.005 & 1.15 \end{bmatrix}$.

In order to measure the performance of the proposed controller, a comparison of the magnitude frequency responses in the open- and closed-loop by implementing the proposed MIMO controller of Fig. 20 is given in Fig. 21. The closed-loop bandwidth increased in the X- and Y-axis are 850 and 775 Hz which is nearly equal to the desired aim of the design process. The amount of damping obtained in the closed-loop for the X- and Y-axis is about 4.5 dB which in turns also reduces the vibration of the scanner. The amount of reduction of cross coupling effects in the intermediate frequency region is higher as compared to low frequency region due to the low gain of the integral controller. However, the magnitude of the cross coupling effects at 10 Hz is less than −45 dB in the both axes which means that both axes can be treated as a independent SISO system.

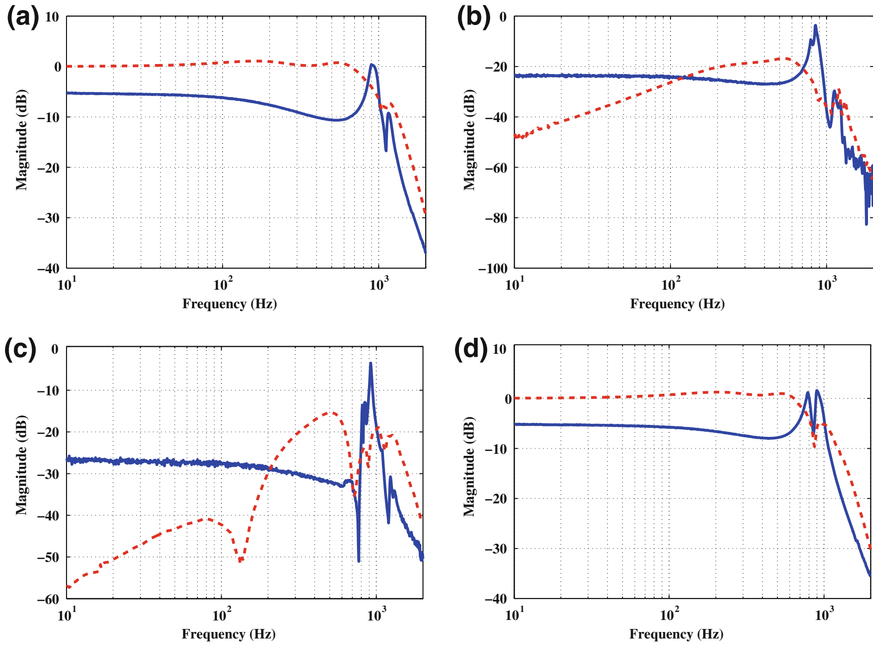

Fig. 21 Comparisons of the Open- and closed-loop magnitude frequency responses (MFRs) relating the inputs $[V_x, V_y]^T$ and the outputs $[D_x, D_y]^T$. The *solid line* (–) represents the measured open-loop MFR and the *dashed line* (- -) represents the measured closed-loop MFR by using the scheme shown in Fig. 20. **a** Magnitude frequency response from Vx to Dx, **b** magnitude frequency response from Vy to Dx, **c** magnitude frequency response from Vx to Dy, and **d** magnitude frequency response from Vy to Dx

9.3 Robustness of the Proposed Controller

The resonance frequency of the piezoelectric tube scanner changes with changing loads. The maximum resonance frequency occurs when there is no load on the scanner. Controllers design for high speed nano-positioning must be able to maintain the closed-loop stability against the changes in resonance frequency which are due to the load change on the scanner. In order to show the performance of the proposed controller in terms of load change on the scanner, a comparison of the open- and closed-loop magnitude frequency responses (MFRs) are given in Fig. 22. The closed-loop MFRs are taken by using the SISO and MIMO double resonant controller in the X-axis of the scanner. As the load on the scanner increases, the resonance frequency of the scanner in the X-axis starts moving towards left, i.e. the resonance frequency of the system decreases. In all cases the closed-loop system remains stable and provides a bandwidth near to the resonance frequency.

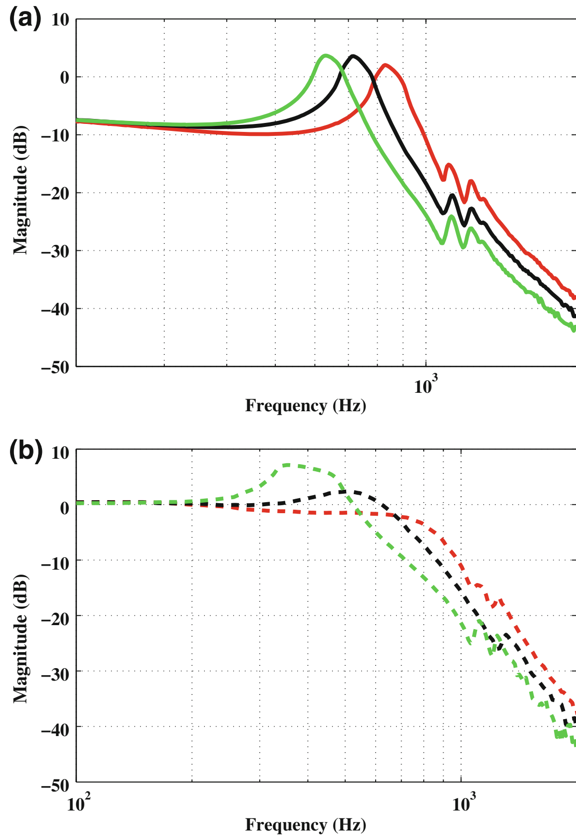

Fig. 22 Open-loop **a** and closed-loop **b** magnitude frequency responses (MFRs) of $G_{xx}(s)$ for different loads on the scanner. The same color in **a** and **b** represents the corresponding open- and closed-loop MFR

10 Image Scanning Results

After improving the lateral positioning of the PTS, investigation is done to evaluate the overall performance of the proposed controller for imaging capability. The experimental images presented in Figs. 23 and 24 show a comparison of the scanned images between the images obtained by implementing the built-in AFM PI controller and the proposed controller of Fig. 20, respectively. The current settings of the AFM used in this paper has no access to measure the gain of the built-in PI controller of the AFM. The software automatically select the gains of the PI controller during the imaging process.

The reference signals applied to the X and Y directions of the piezoelectric tube scanner are generated from the AFM software. The sample used for each imaging is a TGQ1 grating reference sample and the images are taken at scanning rates of 15.62, 31.25, 62.5, and 125 Hz. The structure of the sample is composed of number of squares. From the comparisons of the scanned images it can be observed that the blocks in the scanned images by means of the AFM PI controller are stretched to

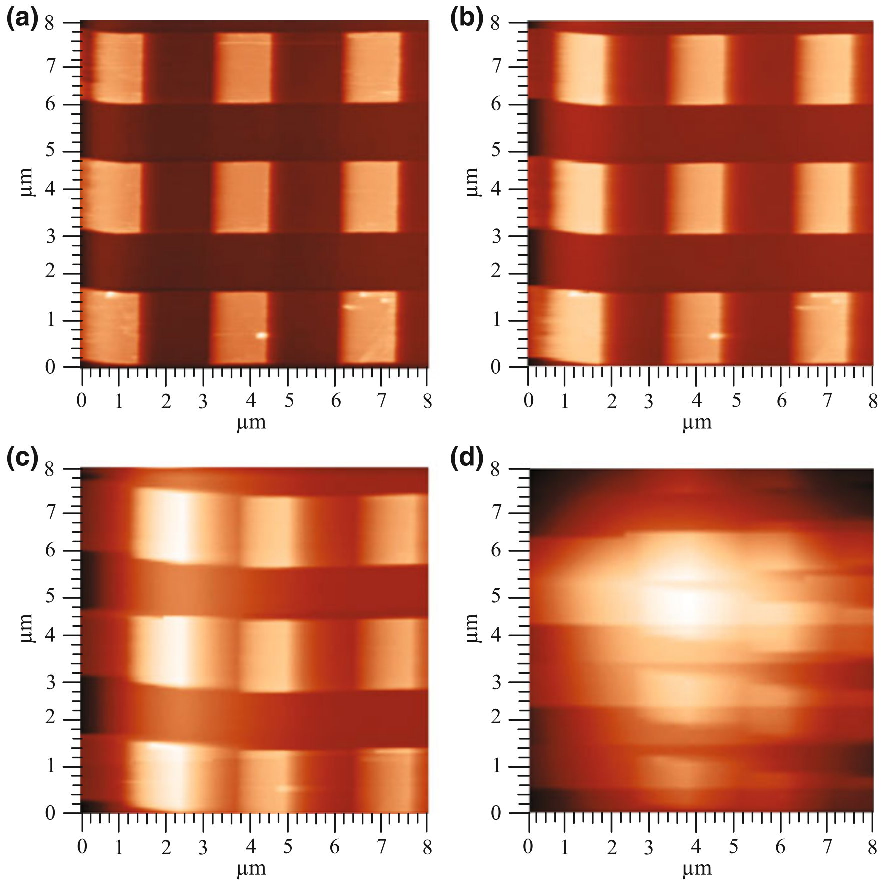

Fig. 23 Scanned images obtained by using the built-in PI controller of the AFM at **a** 15.62, **b** 31.25, **c** 62.5, and **d** 125

the left at low scanning rates. The proposed controller is able to show more uniform blocks at the low scanning frequencies. The scanned images obtained by using of the AFM PI controller are gradually blurred at higher scanning speed. Smother and sharper images are achieved at higher scanning speeds by using the designed controller.

Experimental images shown in Fig. 25 are obtained in open-loop. Note that, the scanned images obtained in open-loop are rotated which are due to the cross coupling effects between the axes of the scanner, whereas the scanned images obtained by using the proposed controller have less rotation. Although, the scanned images obtained by using built-in PI controller of the AFM have less rotation as compared to open-loop scanned images, however, the scanned images obtained by using built-in PI controller of the AFM have distortion at high frequencies which in turn limit the use of built-in PI controller of the AFM.

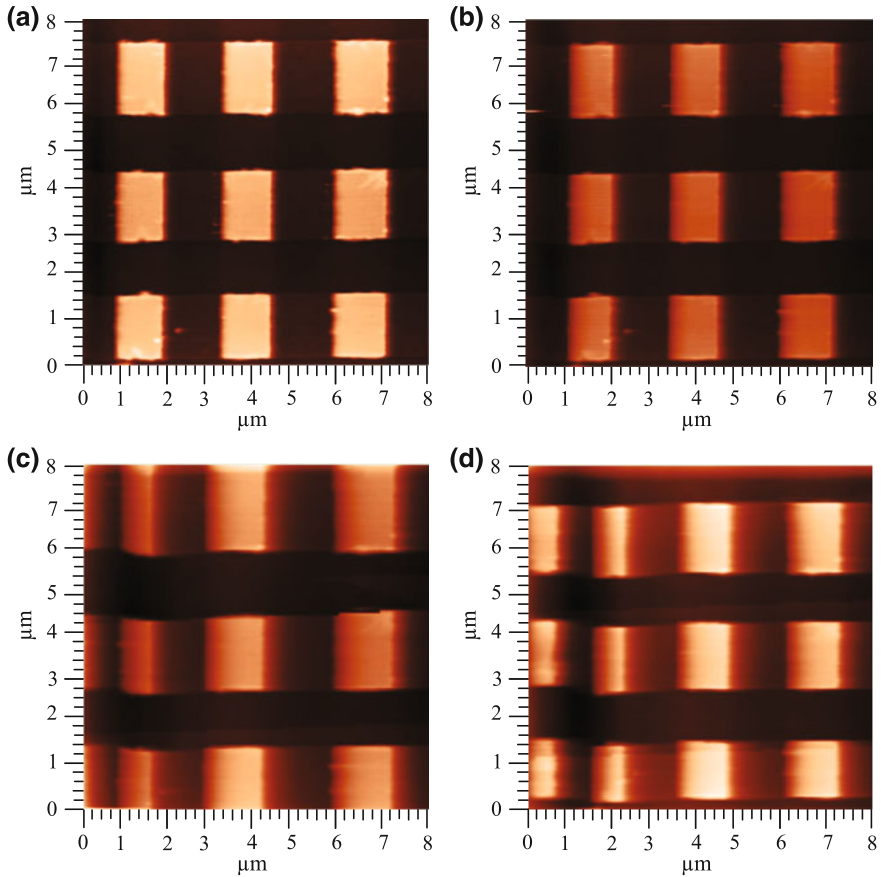

Fig. 24 Scanned images obtained by using the proposed controller at **a** 15.62, **b** 31.25, **c** 62.5, and **d** 125

The comparisons of the tracking performances between the open- and closed-loop for 8 μm × 8 μm area scanning given in Figs. 26 and 27, respectively show that, the proposed controller has a good command over tracking the reference signal at low frequencies whereas the open-loop system is not able to track the reference signal. Although the tracking error increases using the proposed controller at high scanning rate, however, the high closed-loop bandwidth of the proposed controller enables faster scanning as compared to the built-in PI controller of the AFM.

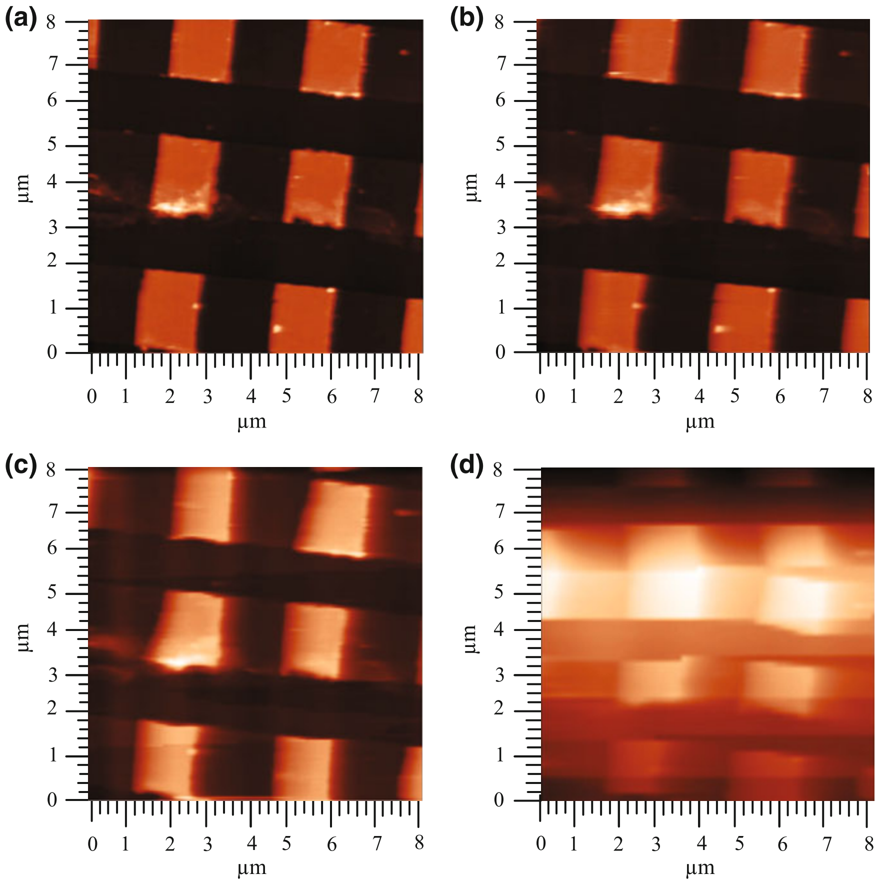

Fig. 25 Open-loop scanned images at **a** 15.62 Hz **b** 31.25 Hz **c** 62.5 Hz and **d** 125 Hz

11 Future Research Directions

This Chapter presents the design of a passive damping controller with a negative-imaginary controller for damping, tracking and cross coupling reduction of a nanopositioner to improve the high speed nanopositioning performance of an AFM. The design of the controller in this Chapter is presented for the X and Y-axis only. The future aim of this work is to incorporate the effect of Z-axis in the controller design.

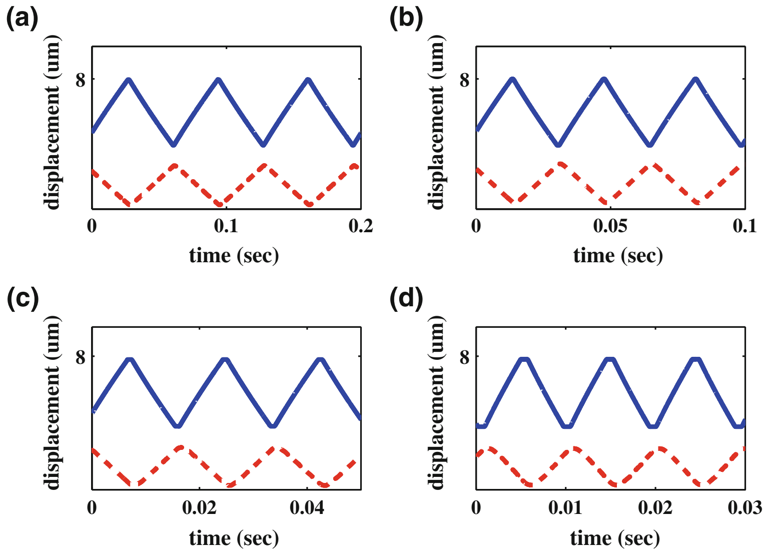

Fig. 26 Open-loop tracking performance at **a** 15.62 Hz, **b** 31.25 Hz, **c** 62.5 Hz and **d** 125 Hz. The *solid line* (–) represents the input signal and the *dashed line* (- -) represents the output signal

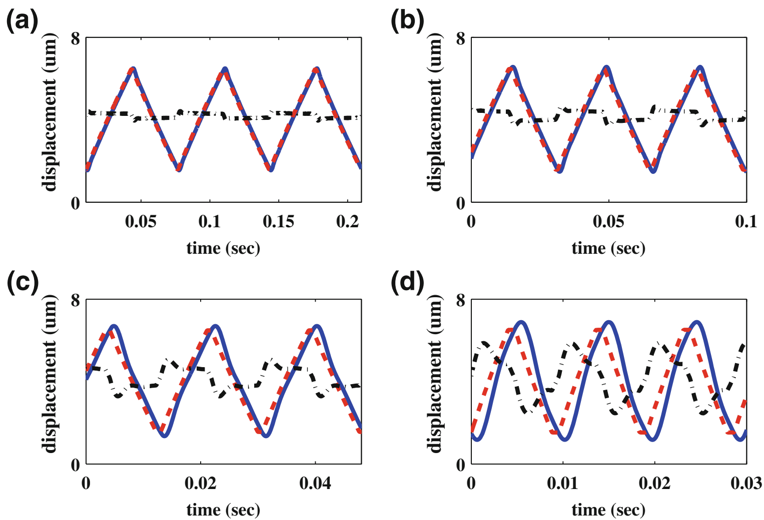

Fig. 27 Closed-loop tracking performance at **a** 15.62 Hz, **b** 31.25 Hz, **c** 62.5 Hz and **d** 125 Hz. The *solid line* (–) represents the input signal, the *dashed* (- -) *line* represents the output signal and the *dashed dot* (-.) *line* represents the error signal between the input and output signal

12 Conclusion

In this Chapter, both SISO and MIMO controllers along with an integral controller are implemented to improve the high speed nanopositioning performance of a PTS by damping the first resonant mode of the PTS, reducing the cross coupling effect between the axes of the PTS, and increasing the bandwidth. Compared to a standard integral controller the proposed controller is able to achieve five times higher bandwidth than the integral controller. The controller design presented in this paper is able to achieve a closed-loop bandwidth near to first resonance frequency of the scanner with a reduction of cross coupling effects. Comparisons of the experimental images presented in the paper obtained by using SISO and MIMO controller show that, the MIMO controller provides substantial improvement in image quality at high scanning rates as compared to the SISO controller.

References

1. Adriaens, H., De Koning, W., Banning, R.: Modeling piezoelectric actuators. IEEE/ASME Trans. Mechatron **5**(4), 331–341 (2000)
2. Al Janaideh, M., Rakheja, S., Su, C.Y.: An analytical generalized Prandtl-Ishlinskii model inversion for hysteresis compensation in micropositioning control. IEEE/ASME Trans. Mechatron. **16**(4), 734–744 (2011)
3. Amelio, S., Goldade, A.V., Rabe, U., Scherer, V., Bhushan, B.: Measurments of mechanical propoerties of ultra-thin diamond-like carbon coatings using atomic force acoustic microscopy. Thin Solid Films **392**, 75–84 (2001)
4. Ando T, Uchihashi T, Kodera N, Yamamoto D, Taniguchi M, Miyagi A, Yamashita H.: High-speed Atomic Force Microscopy for Nano-visualization of Biomolecular Processes. Wiley-VCH Verlag GmbH & Co. KGaA. pp. 277–296 (2009)
5. Ang WT, Garmon F, Khosla P, Riviere C.: Modeling rate-dependent hysteresis in piezoelectric actuators. In: Proceedings. 2003 IEEE/RSJ International Conference on Intelligent Robots and Systems, 2003 (IROS 2003), vol. 2, pp. 1975–1980 (2003)
6. Balas, M.J.: Direct velocity feedback control of large space structures. J. Guidance Control **2** (3), 252–253 (1979)
7. Barbara, P.F., Adams, D.M., O'Connor, D.B.: Characterization of organic thin film materials with near-field scanning optical microscopy. Annu. Rev. Mater. Sci. **29**, 433–469 (1999)
8. Betzig, E., Finn, P.L., Weiner, J.S.: Combined shear force and near-field scanning optical microscopy. Appl. Phys. Lett. **60**(20), 2484–2486 (1992)
9. Bhikkaji B, Yong YK, Mahmood IA, Moheimani SR.: Multivariable Control Designs for Piezoelectric Tubes. In: Proceedings of the 18th IFAC World Congress. August 28–September 2, vol. 18. Milano, Italy (2011)
10. Bhikkaji, B., Moheimani, S.O.: Integral Resonant Control of a Piezoelectric Tube Actuator for Fast Nanoscale Positioning. IEEE/ASME Trans. Mech. **13**(5), 530–537 (2008)
11. Bhikkaji, B., Ratnam, M., Fleming, A.J., Moheimani, S.O.R.: High-Performance Control of Piezoelectric Tube Scanners. IEEE Trans. Control Sys. Tech. **15**(5), 853–866 (2007)
12. Binnig, G., Rohrer, H.: American Physical Society; Scanning tunneling microscopy from birth to adolescence. Rev. Mod. Phys. **59**, 615–625 (1987)
13. Binnig, G., Smith, D.P.E.: Single-tube three-dimensional scanner for scanning tunneling microscopy. Rev. Sci. Instrum. **57**(8), 1688–1689 (1986)

14. Binnig, G., Quate, C.F., Gerber, C.: American Physical Society; Atomic Force Microscope. Phys. Rev. Lett. **56**, 930–933 (1986)
15. Binnig, G., Quate, C.F., Gerber, C.: American Physical Society; Atomic Force Microscope 2D and 3D. Phys. Rev. Lett. **56**, 930–933 (1986)
16. Croft D, Shedd G, Devasia S.: Creep, hysteresis, and vibration compensation for piezoactuators: atomic force microscopy application. In: Proceedings of American Control Conference, pp. 2123–2128 (2000)
17. Das SK, Pota HR, Petersen IR. Damping controller design for nanopositioners: a mixed passivity, negative-imaginary and small-gain approach. IEEE/ASME Trans. Mechatronics (2014, In Press)
18. Das SK, Pota HR, Petersen IR.: Multi-variable Double Resonant Controller for Fast Image Scanning of Atomic Force Microscope, Asian Control Conference, Washington, 23–26 June 2013, pp. 1–6. Istanbul (2013b)
19. Das SK, Pota HR, Petersen IR.: Multi-variable Resonant Controller for Fast Atomic Force Microscopy. In: Proceedings of Australian Control Conference. pp. 448–453. Sydney, Australia (2012b)
20. Das SK, Pota HR, Petersen IR.: Resonant control of atomic force microscope scanner: A "mixed" negative-imaginary and small-gain approach. In: American Control Conference, Washington, June 17–19, 2013, pp. 5476–5481. Washington DC, USA (2013a)
21. Das SK, Pota HR, Petersen IR.: Resonant controller design for a piezoelectric tube scanner: a mixed negative-imaginary and small-gain approach. IEEE Trans. Control Syst. Technol. (2013c, In Press)
22. Das SK, Pota HR, Petersen IR.: Resonant Controller for Fast Atomic Force Microscopy. In: Proceedings of Conference on Decision and Control. pp. 2471–2476. Maui, Hawaii (2012a)
23. Devasia, S., Eleftheriou, E., Moheimani, S.: A Survey of Control Issues in Nanopositioning. IEEE Trans. Control Sys. Tech. **15**(5), 802–823 (2007)
24. DeVecchio, D., Bhushan, B.: Use of a nanoscale Kelvin probe for detecting wear precursors. Rev. Sci. Instrum. **69**(10), 3618–3624 (1998)
25. El Rifai OM, Youcef-Toumi K.: Coupling in piezoelectric tube scanners used in scanning probe microscopes. In: Proceedings of American Control Conference the 2001, vol. 4, pp. 3251–3255 (2001)
26. Fleming, A.J.: Nanopositioning system with force feedback for high-performance tracking and vibration control. IEEE/ASME Trans. Mechatron. **15**(3), 433–447 (2010)
27. Fleming AJ, Leang KK.: Evaluation of charge drives for scanning probe microscope positioning stages. In: Proceedings of American Control Conference, pp. 2028–2033 (2008)
28. Fleming, A.J., Moheimani, S.O.R.: Precision current and charge amplifiers for driving highly capacitive piezoelectric loads. Electron. Lett. **39**(3), 282–284 (2003)
29. Fleming, A.J., Aphale, S.S., Moheimani, S.O.R.: A New Method for Robust Damping and Tracking Control of Scanning Probe Microscope Positioning Stages. IEEE Trans. Nanotechnology **9**(4), 438–448 (2010)
30. Hansma, P., Drake, B., Marti, O., Gould, S., Prater, C.: The scanning ion-conductance microscope. Science **243**(4891), 641–643 (1989)
31. Hartmann, U.: Magnetic force microscopy. Annu. Rev. Mater. Sci. **29**, 53–87 (1999)
32. Hung, S.K.: Spiral Scanning Method for Atomic Force Microscopy. J. Nanosci. Nanotechnol. **10**, 4511–4516 (2010)
33. Husser, O.E., Craston, D.H., Bard, A.J.: Scanning eletromechanical microscopy-high resolution deposition and etching materials. J. Electrochem. Soc. **136**, 3222–3229 (1989)
34. Ikhouane, F., Manosa, V., Rodellar, J.: Dynamic properties of the hysteretic Bouc-Wen model. Syst. Control Lett. **56**(3), 197–205 (2007)
35. Kuhnen, K., Krejci, P.: Compensation of complex hysteresis and creep effects in piezoelectrically actuated systems—a new Preisach modeling approach. IEEE Trans. Autom. Control **54**(3), 537–550 (2009)

36. Leang, K.K., Devasia, S.: Feedback-Linearized Inverse Feedforward for Creep, Hysteresis, and Vibration Compensation in AFM Piezoactuators. IEEE Trans. Control Syst. Technol. **15** (5), 927–935 (2007)
37. Lee, D.T., Pelz, J.P., Bhushan, B.: Instrumentation for direct, low frequency scanning capacitance microscopy, and analysis of position dependent stray capacitance. Rev. Sci. Instrum. **73**, 3523–3533 (2002)
38. Green M, Limebeer DJN.: Linear Robust Control. Prentice-Hall, NJ (1995)
39. Mahmood, I.A., Moheimani, S.O.R.: Making a commercial atomic force microscope more accurate and faster using positive position feedback control. Rev. of Sci. Instrum. **80**(6), 063705(1)–063705(8) (2009)
40. Majumdar, A.: Scanning thermal microscopy. Annu. Rev. Mater. Sci. **29**, 505–585 (1999)
41. Matey, J., Blanc, J.: Scanning capacitance microscopy. Annu. Rev. Mater. Sci. **57**, 1437–1444 (1999)
42. McKelvey, T., Akay, H., Ljung, L.: Subspace-based identification of infinite-dimensional multivariable systems from frequency-response data. Automatica **32**(6), 885–902 (1996)
43. Melitz, W., Shen, J., Kummel, A.C., Lee, S.: Kelvin probe force microscopy and its application. Surf. Sci. Rep. **66**(1), 1–27 (2011)
44. Patra, S., Lanzon, A.: Stability Analysis of Interconnected Systems With "Mixed" Negative-Imaginary and Small-Gain Properties. IEEE Trans. Autom. Control **56**(6), 1395–1400 (2011)
45. Petersen IR.: Negative imaginary systems theory in the robust control of highly resonant flexible structures. In: Australian Control Conference. Melbourne, Australia. pp. 1–6 (2011)
46. Petersen, I., Lanzon, A.: Feedback Control of Negative-Imaginary Systems. IEEE Control Sys. Mag. **30**(5), 54–72 (2010)
47. Pota H, Moheimani SR, Smith M.: Resonant controllers for flexible structures. In: Proceedings Conference of Decision and Control, vol. 1. pp. 631–636 (1999)
48. Pota, H., Reza Moheimani, S., Smith, M.: Resonant controller for smart structures. Smart Mater. Struct. **11**, 1–8 (2002)
49. Prater, C., Hansma, P., Tortonese, M., Quate, C.: Improved scanning ion-conductance microscope using microfabricated probes. Rev. Sci. Instrum. **62**(11), 2634–2638 (1991)
50. Ratnam M, Bhikkaji B, Fleming A, Moheimani S. PPF Control of a Piezoelectric Tube Scanner. In: 44th IEEE Conference on Decision and Control and European Control Conference, pp. 1168–1173 (2005)
51. Rost, M.J., vanBaarle, G.J.C., Katan, A.J., vanSpengen, W.M., Schakel, P., vanLoo, W.A., Oosterkamp, T.H., Frenken, J.W.M.: John Wiley and Sons Asia Pte Ltd; Video-rate scanning probe control challenges: setting the stage for a microscopy revolution. Asian J. Control **11**(2), 110–129 (2009)
52. Salapaka, S., Sebastian, A., Cleveland, J.P., Salapaka, M.V.: High bandwidth nano-positioner: A robust control approach. Rev. Sci. Instrum. **73**(9), 3232–3241 (2002)
53. Scherer, V., Arnold, W., Bhushan, B.: John Wiley & Sons, Ltd.; Lateral force microscopy using acoustic friction force microscopy. Surf. Interface Anal. **27**(5–6), 578–587 (1999)
54. Schitter G, Astrom KJ, DeMartini B, Fantner GE, Turner K, Thurner PJ, Hansma PK. Design and modeling of a high-speed scanner for atomic force microscopy. In: Proceedings of American Control Conference (2006)
55. Schitter G, Rost MJ. Scanning probe microscopy at video-rate. Mater. Today **11**(0), 40–48 (2008)
56. Schitter G, Stemmer A, Allgower F. Robust 2 DOF-control of a piezoelectric tube scanner for high speed atomic force microscopy. In: Proceedings of American Control Conference the 2003, vol. 5, pp. 3720–3725 (2003)
57. Schitter, G., Menold, P., Knapp, H.F., Allgöwer, F., Stemmer, A.: High performance feedback for fast scanning atomic force microscopes. Rev. Sci. Instrum. **8**, 72 (2001)
58. Schoenenberger, C., Alvarado, S.: Springer, Understanding magnetic force microscopy. Z. Phys. **80**(3), 373–383 (1990)

59. Sebastian A, Salapaka MV, Cleveland JP.: Robust control approach to atomic force microscopy. In: Proceedings of 42nd IEEE Conference on Decision and Control, vol. 4, pp. 3443–3444 (2003)
60. Sebastian, A., Salapaka, S.M.: Design methodologies for robust nano-positioning. IEEE Trans. on Control Sys. Tech. **13**(6), 868–876 (2005)
61. Stern, J.E., Terris, B., Mamin, H., Rugar, D.: Deposition and imaging of localized charge on insulator surfaces using a force microscope. Appl. Phys. Lett. **53**(26), 2717–2719 (1988)
62. Tuma, T., Lygeros, J., Kartik, V., Sebastian, A., Pantazi, A.: High-speed multiresolution scanning probe microscopy based on Lissajous scan trajectories. Nanotechnology **23**(18), 185501 (2012)
63. Williams, C., Wickramasinghe, H.: Scanning thermal profiler. Appl. Phys. Lett. **49**(23), 1587–1589 (1986)
64. Williams, C.C., Wickramasinghe, H.K.: Microscopy of chemical-potential variations on an atomic scale. Nature **344**, 317–319 (1990)
65. Yong YK, Moheimani SOR, Petersen IR. 2010. High-speed cycloid-scan atomic force microscopy. Nanotechnology 21(36)